Infrared Thermography for In-pile Imaging of Nuclear Fuel Cracking

Thesis

Presented in Partial Fulfillment of the Requirements for the Degree Master of Science in the
Graduate School of The Ohio State University

By

Kevin Agarwal

Graduate Program in Mechanical Engineering

The Ohio State University

2019

Thesis Committee

Dr. Marat Khafizov, Advisor

Dr. Carol Smidts

Abstract

The objective of this article is to present Infrared Thermography (IRT) methodology and results for crack detection in nuclear fuel in-pile in a reactor environment and under laboratory conditions. Cracking of nuclear fuel has notable implications on the fuel performance. Cracks provide a pathway for faster fission gas release and buildup of pressure inside the fuel rod. Crack induced relocation of fuel results in pellet cladding mechanical interaction. Lastly the fragmentation of the fuel under severe thermal stress leads to loss of fuel ability to maintain coolable geometry. The aforementioned phenomena impact the life time of the fuel. In-situ detection of the solid material cracking will allow for better understanding of the fuel's thermo-mechanical behavior and allow validation and development of advanced fuel performance codes. In this article, we summarize the result of the modeling efforts to identify an optimal configuration for IRT imaging to detect the structural evolution of fuel. Similar approaches can be further expanded and consider fuel void formation, relocation and pellet cladding interaction. In this modeling effort, various heater configurations including source and geometry as well as ambient temperature conditions were considered. A setup with optical IR fiber bundles implementing IR camera with lock-in detection capability has been identified as a first step for achieving in-pile implementation. The ability to detect cracks in-pile will open up possibilities for further advancements in enhancing fuel performance.

Acknowledgments

First, I would like to thank and express my gratitude to Dr. Marat Khafizov for giving me an opportunity to work on an intriguing problem and conduct research under his guidance. He has not only guided me through my research, but has also been a great mentor encouraging me through all the difficulties I faced throughout my masters program at The Ohio State University. I would like to sincerely thank Dr. Carol Smidts for serving on my thesis committee. I am grateful for her support and time to guide me on various aspects of the research and graduate program. Special thanks to Dr. Colby Jensen, Dr. Robert Schley and Dr. David Hurley for inspiring this research and providing me with insightful technical feedback. I would also like to acknowledge the assistance of Dr. Nirmala Kandadai, Dr. Harish Subbaraman for providing me with the experimental feedback. I would also like to extend my sincere thanks to Vinay Chauhan, Yuzhou Wang and Gaofeng Sha for their constant support and help in various research problems. Last but not the least, I would like to thank my family and friends at The Ohio State university for standing by me throughout my life

Vita

2013………………………………………	B.E. (Hons), Mechanical Engineering, BITS Pilani, Goa Campus
2017 to present…………………………....	M.S. Mechanical Engineering, The Ohio State University

Fields of Study

Major Field: Mechanical Engineering

Table of Contents

List of Tables

List of Figures

Chapter 1: INTRODUCTION

1.1 Infrared Thermography for Non Destructive Testing

Infrared Thermography (IRT) is an emerging Non Destructive Technique (NDT) which allows for the non-contact inspection of systems and materials. The monitoring is achieved through a mapping of thermal pattern on the surface of interest. IRT detection is based on the fact that there exists a difference in thermal properties and patterns between the defective and the non-defective areas, which can be used for identifying and quantifying the defects.

IRT for NDT finds applications in aerospace, medical, nuclear, automotive and many other fields. Applications of IRT for inspection of rotor blades and detecting loose connections in an electrical circuit is shown in Figure 1. For the inspection of rotor blades the rotor with bright areas indicates the delamination produced by heat due to friction of micro cracks [1]. Moreover the loose connections in an electrical circuit lead to costs associated with manufacturing downtime, production losses, power outages, fires and catastrophic failures. Here, IRT enhances the ability to predict equipment failure and plan corrective action before a costly shutdown, equipment damage, or personal injury occurs.

Applications of IRT for NDT applications can be further extended for in reactor fuel behavior monitoring [2], [3], [4]. The importance and need for achieving of in-reactor fuel monitoring is presented in the subsequent section.

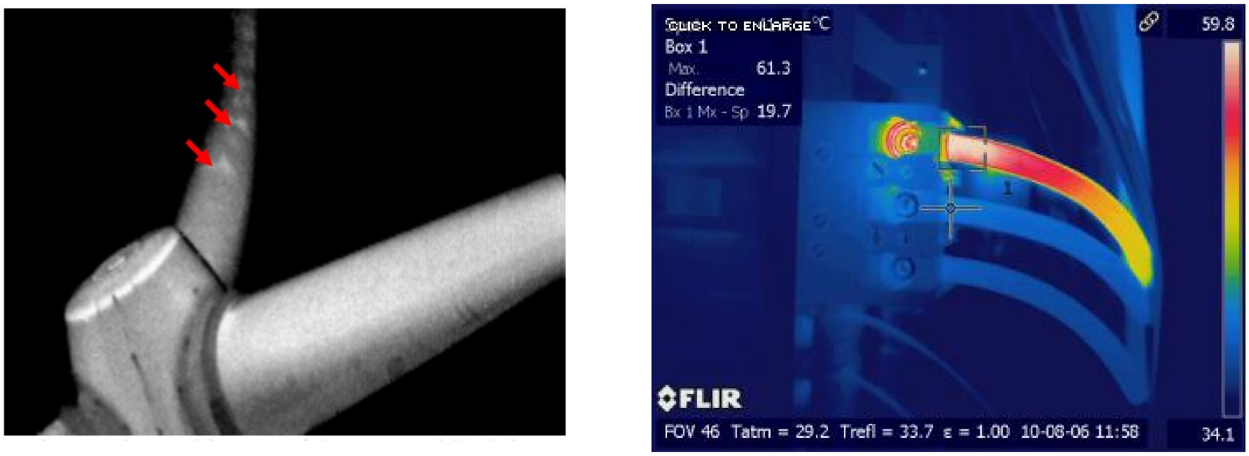

Figure 1: Thermal image of rotor blades with delamination [1] (left), Thermal image of electrical circuit with loose connection failure (FLIR) (right)

1.2 Thermal and Structural behavior of nuclear fuel rod

Early in life of a nuclear fuel, thermal gradients are induced due to initial power ramps. The large thermal gradients cause high tensile hoop and axial stresses in outer region of fuel pellets, resulting in formation of radial and axial cracks. Circumferential cracks are caused due to the ramping down of power. Such structural changes can occur in the first few moments of startup or may happen from months to years. Figure 2 (left) shows a sample of UO_2 fuel cross-section, from a fuel rod that has seen a reactor power excursion of 42 kW/m^2 [5]. These structural changes and cracks cause the fuel to expand radially, narrowing the pellet/cladding gap and essentially decreasing effective conductivity of the fuel in direction normal to cracking [6], [7]. Figure 2 (right) illustrates the crack patterns for increasing rod powers. The figure clearly shows an increase in number of pellet fragments for every surge in rod power [6].

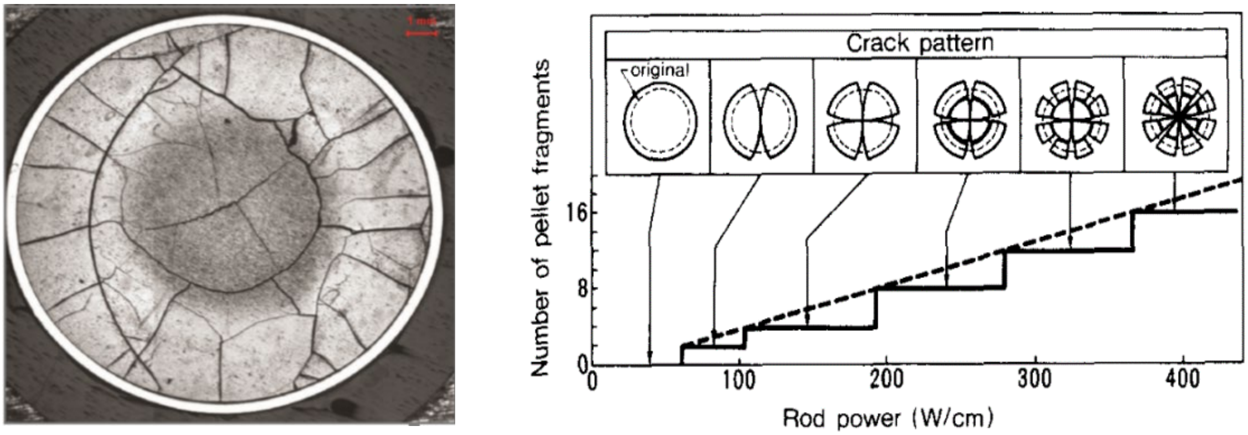

Figure 2: Fuel Cross Section of UO2 nuclear fuel post irradiation [5] (left), Changes in crack pattern and fragmentation during a surge in the rod power [6] (right)

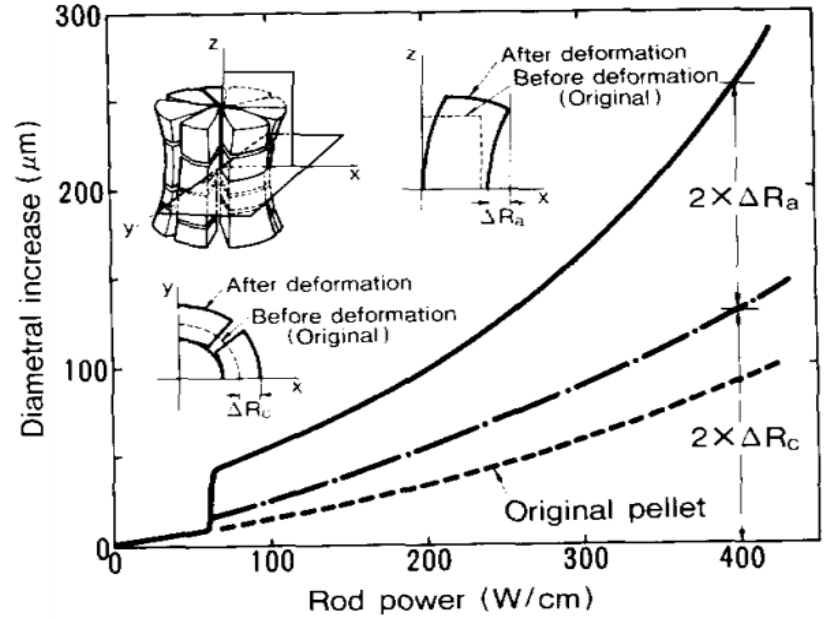

Figure 3: Diametric increase of cracked pellet during a surge in rod power [6]

Another factor that accompanies the fuel fracture is fuel relocation that increases the apparent pellet diameter. Figure 3 shows the effective diameter increase with the increase in the rod power [6]. As the pellet cracks, the fragments become larger than the original pellet radius and the apparent diameter of the cracked pellet increases accordingly. As the pellet clad diameter increases it leads to the fuel-cladding mechanical interaction. The fuel cladding interaction is of great importance for predicting the fuel performance behavior and is a complex, multi diffusion problem. Fuel cladding interaction results in weakening of the cladding and formation of low melting point compositions in the fuel [8]. Figure 4 shows the fuel cladding chemical interaction on the inner side of the clad [9].

The formation of central voids is another important phenomenon that occurs inside the nuclear fuel rods following the initial power ramp. High thermal stresses and temperature gradients following the power ramp cause atomic transport leading to the void movement inside the fuel. As the voids move up the gradient, they coalesce in the fuel interior leading to the formation of a large central void. Fission gas release, creep, thermal conductivity are parameters strongly linked to the motions and growth kinetics of the central void. Due to its high importance a number of studies have been conducted focusing on modelling of the central voids [10].

Additionally research on a number of modelling approaches has been performed to study the important effects that fracture has on the fuel performance [6], [11]. The discrete element method (DEM) approach aims to model the thermally induced fracture in ceramic nuclear fuel. Initially the DEM fuel pellet model simulation was performed on un-fractured fuels to witness the thermal and the mechanical response. Figure 5 shows the temperature and hoop stress fields predicted by the DEM model without fracturing after a linearly increasing ramp from zero power to a full power of 25 kW/m over 10000 s [11]. A maximum temperature of 1400 K is observed at the middle of the fuel with a maximum hoop stress of 800 MPa towards the periphery of the hoop.

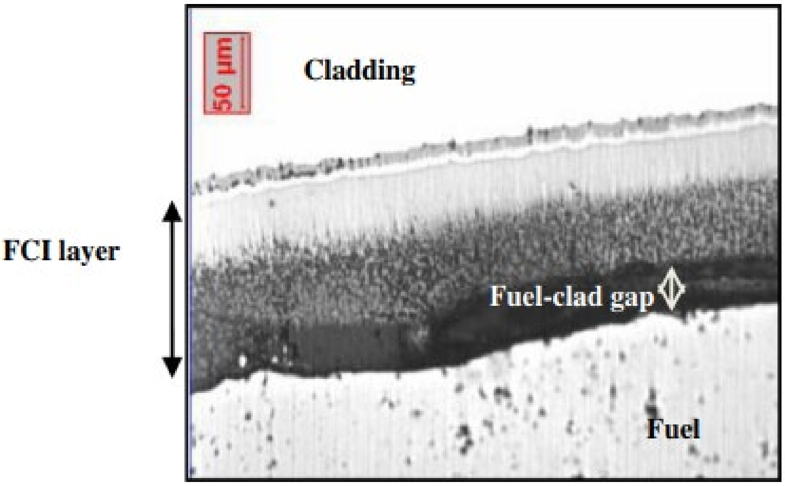

Figure 4: Oxide layer and fuel-clad interaction layer on the inner side of the clad [9]

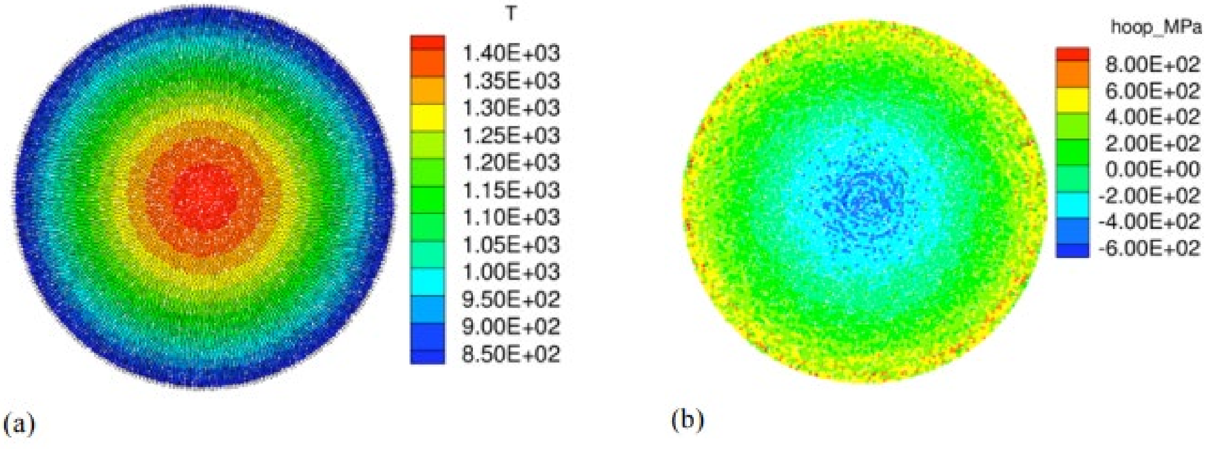

Figure 5: Results of DEM simulation of fuel pellet without fracturing following rise to 25kW/m power showing (a) Temperature field (K) (b) Hoop stress field (MPa) [11]

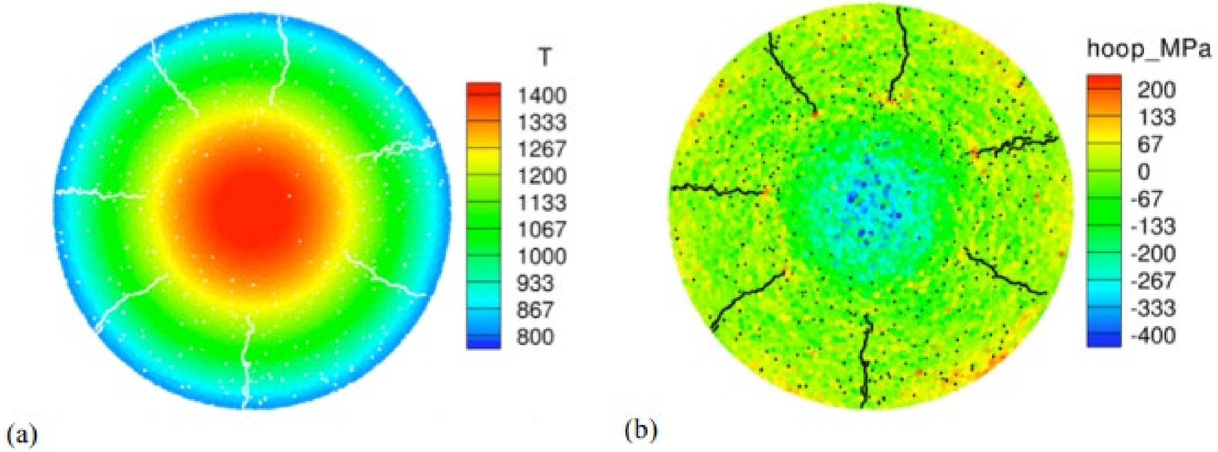

Figure 6: Results of DEM simulation with fracturing after rise to 25 kW/m rod power, (a) Temperature (K), (b) Hoop Stress (MPa) [11]

Figure 6 shows the DEM fuel pellet model with fuel fracturing [11]. Under this model no heat conduction is permitted across the broken bonds. On comparing the hoop stresses shown in Figures 5 and 6, for the uncracked case the high hoop stresses in the periphery and the exterior are relieved by the cracking and the compressive stresses are reduced as well. It is also important to note that in this case when the cracking is primarily radial, the heat flows parallel to the cracks and hence the presence of cracks has little influence on the temperature field. Overall the fractures inside a nuclear fuel rod have a very strong influence on the stress state in the fuel which, in turn, drives critical phenomena such as fission gas release, fuel creep, and eventual fuel/clad mechanical interaction while affect the fuel performance. Hence because of the influence that fracture has on fuel performance, in reactor monitoring of fuel behaviors becomes important. Since thermal conductivity has a direct impact on the aferomentioned behavior, a number of studies have been conducted to understand the thermal conductivity of nuclear fuels [12].

1.3 Neutron radiography for inspection of irradiated nuclear fuel rods

Historically, inspection and testing of irradiated nuclear fuel rods has been performed using techniques such as X-ray imaging, gamma-ray imaging and neutron radiography. Among these, neutron radiography has been found to have several advantages over X-ray and the gamma-ray radiographic techniques [13], [14]. The principle of neutron radiography is that a beam of neutrons passes through the work piece to be examined and exposes a suitable convertor screen which further emits detectable radiation to form a radiographic image. The schematic of the general radiographic process is shown in Figure 7 [15]. Neutron radiography uses thermal neutrons as source of radiation. Figure 8 shows neutron radiographs of irradiated nuclear fuel indicating random cracks in pellets [15]. The radiography shows valuable information regarding the condition of nuclear fuel such as fuel swelling, pellet-clad interactions, pellet cracking, fuel void formation, pellet-clad and pellet-pellet gaps etc.

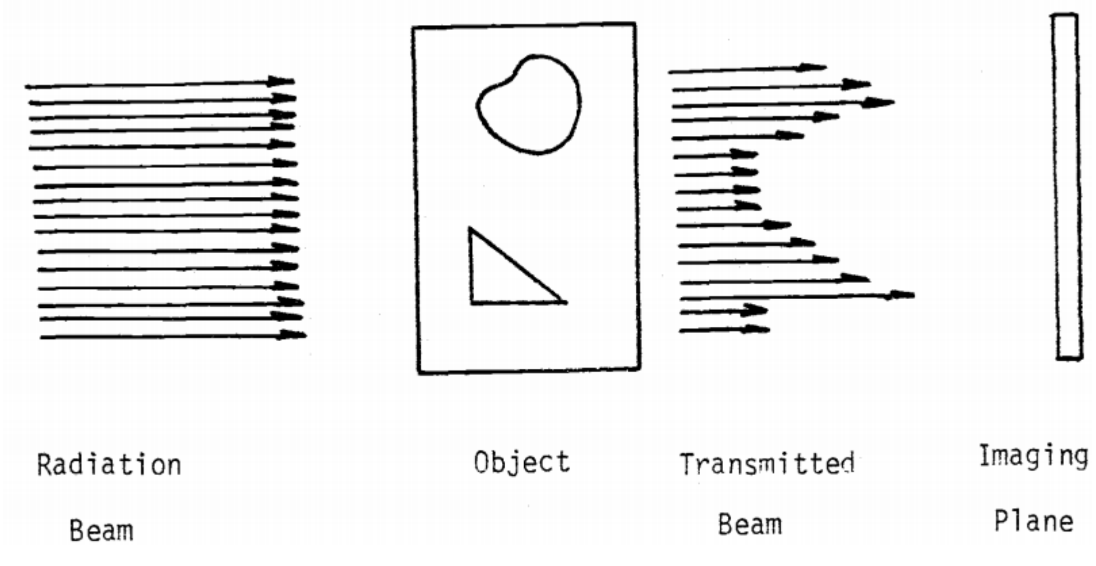

Figure 7: General Radiographic Process [15]

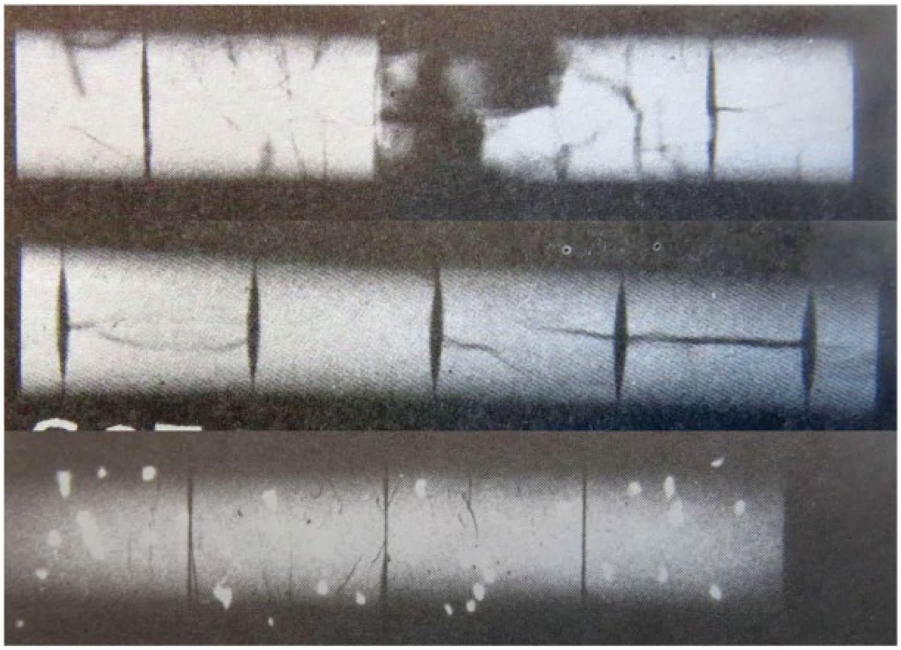

Figure 8: Neutron radiographs (film prints) of irradiated nuclear fuel and their conditions [15]

Despite the advantages offered by Neutron Radiography, a major limitation is that radiation safety precautions must be used i.e. there is a potential radiation hazard that requires the personnel to be properly equipped and organized to handle radiation and radioactive material. Additional care must be taken with all components that have been exposed in the neutron beam, including the inspection objects that may exhibit some level of radioactivity due to neutron activity. Presently there are presently just a few number of facilities for performing neutron radiography and only a small number of people have been certified as Level 3 in neutron radiography. Due to the challenges and the limitations offered by radiography techniques, IRT offers a potential for inspection of irradiated nuclear fuel rods [16], [17], [18], [19]. The advantages offered by IRT for monitoring of in reactor fuel behavior are as follows: -

- Understanding that IRT is a non-contact technique, it requires only optical access to the object while displaying real time images whose signal strength increases with increasing temperature.
- IRT provides real time two-dimensional thermal images which makes is possible for defect detection in real time and at a much faster rate.
- IRT has no harmful effects of technologies such as X-ray imaging or neutron imaging and it does not intrude with the target in any way.

For developing IRT for in-reactor monitoring one of the most important issues to be addressed is identifying an optimal IRT configuration and components for detecting specific structural evolutions such as fuel cracking and void formations. IRT and its different technique variations have been summarized in the following section.

1.4 Infrared Thermography Technique Variations

Infrared Thermography is divided into two approaches namely the passive and active approaches. Passive thermography is used when the object of interest has sufficient thermal contrast with respect to the background in order to be detected by the infrared sensor. Applications for passive thermography include: - insulation and leakage problems, humidity assessment in buildings, public services (forest fire detection, road traffic monitoring), maintenance (bearings, turbine blades, electric installations, pipelines). Figure 9 shows a thermal image for fire detection using an IR camera (Dias – Infrared Systems). IRT makes fire detection possible even in poorer weather conditions and poorer visibility conditions when the detection is not possible using the naked eye. In contrast to the passive approach, active infrared thermography requires an external source of energy to induce a thermal contrast or a temperature difference between the defective and the non-defective areas under examination. Figure 10 illustrates a wide variety of active infrared thermography approaches on the basis of the excitation methodologies, [20].

Figure 9: Passive Thermography for Long Range Fire Detection (Dias – Infrared Systems)

As illustrated in Figure 10 [20], different forms of excitation methodologies are possible namely: optical external excitation, electromagnetic internal excitation, mechanical internal excitation etc. Under optical external excitation the heating is achieved through the means of pulsed heat simulation (Pulsed thermography) or periodic heating (Lock in thermography). Here the energy is received on the external surface of the specimen in the form on heat. The thermal waves propagate through the specimen through conduction until they reach a discontinuity where the thermal waves either slow down or speed up depending upon the thermal properties of the specimen or the discontinuity.

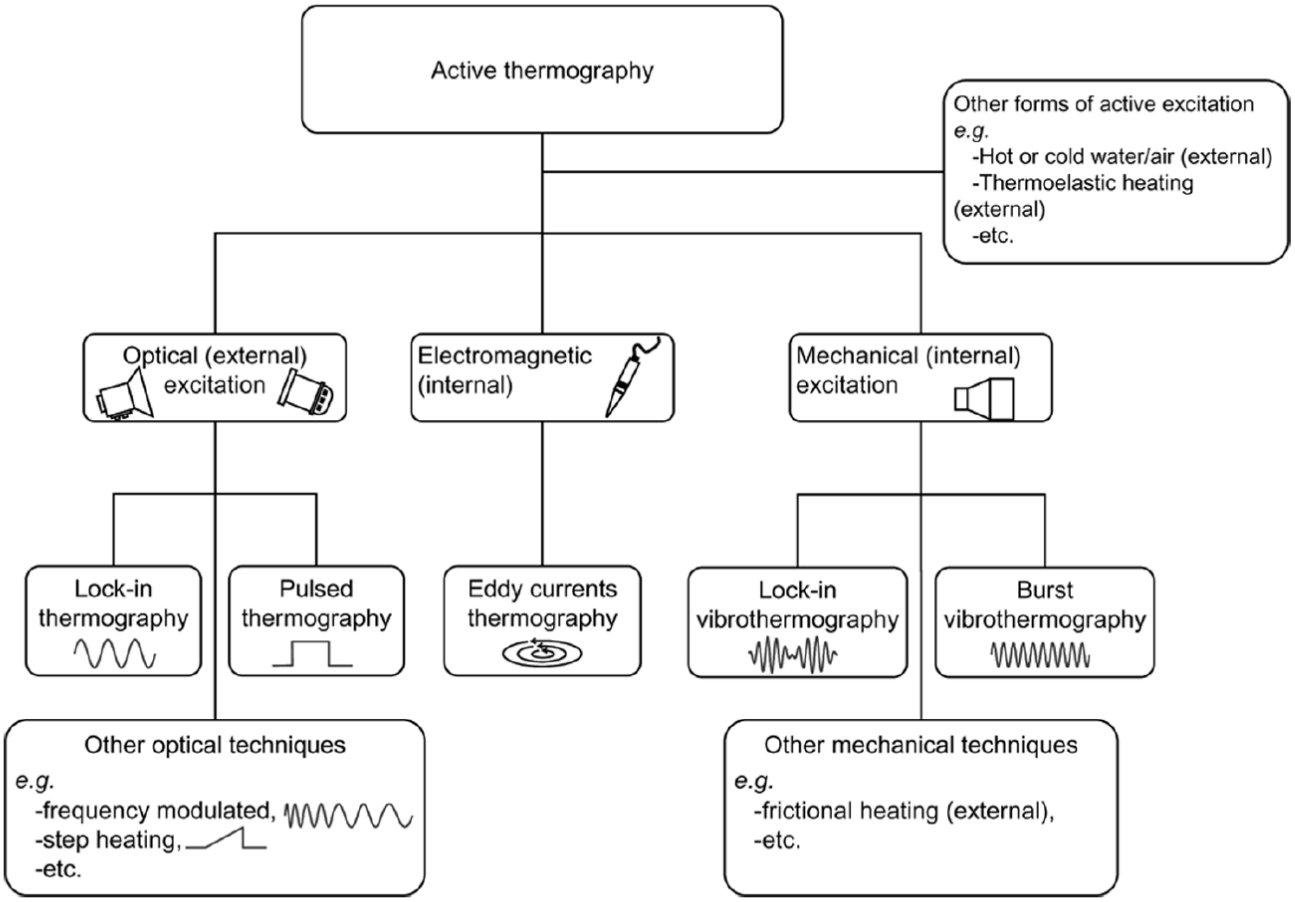

Figure 10: Active infrared thermography approaches [20]

Schematic of the optical techniques is shown in Figure 11 [20]. A brief overview of pulsed thermography and lock in thermography is presented below: -

Pulsed Thermography (PT): - PT is one of the most popular active IRT techniques and has a relatively quick application time. PT does not require physical contact with the specimen being inspected. Under PT a heat pulse is applied to the object of interest for a fraction of second while using an IR camera to monitor the temperature decay curve of the surface as heat travels through the material. Here the heat source can be a flash lamp, halogen lights, heating gun, hair dryer or laser beams. PT does however have a lot of drawbacks, such as reflections from the environment, emissivity variations, non uniform heating and surface geometry variations. NDT using PT finds application for specific defect detection [21], restoration of art [22], inspection of wind turbine blades [23]etc.

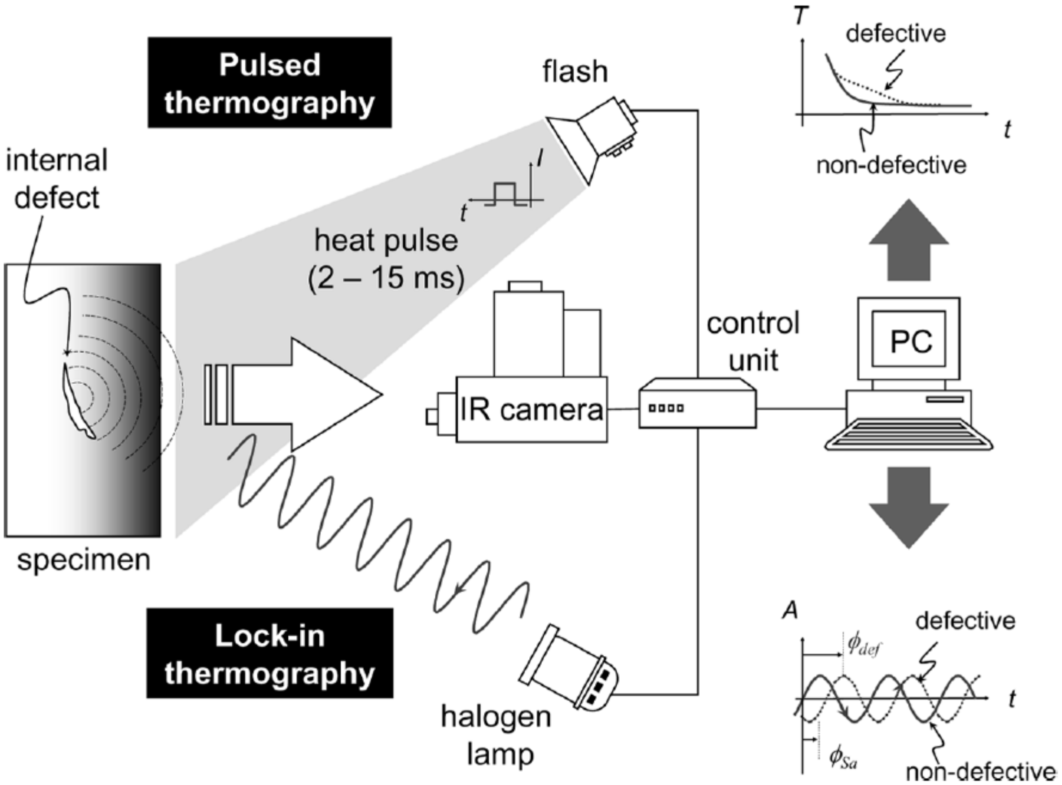

Figure 11: Schematic Diagram of Pulsed Thermography and Lock In Thermography [20]

<u>Lock in Thermography (LIT)</u>: - In LIT, thermal energy is delivered to the specimen's surface in the form of a modulated thermal waves and the thermal images are captured under the periodic sinusoidal heating. The modulated frequency of the periodic heater determines the thermal

diffusion length and is optimized to obtain thermal contrast across the crack. LIT uses amplitude and the phase measurements for assessment of the underlying defects and its parameters such as size, depth and its thermal resistance through analysis of the measured profile’s amplitude. Amplitude images display the total temperature increase on the system and the phase image represents the time delay between powering a device and subsequent heating of the surface. Amplitude images are analyzed to determine the defect shape and size while the phase image for defect depth. NDT using LIT finds applications for crack detection [24], [25], [26], investigation of solar modules [27], failure analysis of integrated circuits [28] etc.

Under mechanical internal excitation, the energy is delivered through means of mechanical oscillations using a sonic or ultra-sonic transducer. Here the heating is achieved internally, i.e. mechanical oscillations injected into the specimen spread into all directions dissipating their energy at the discontinuities in the form of heat, which travel to the surface by conduction. A brief overview of lock in vibro-thermography is presented below: -

Lock in Vibrothermography: - Under vibrothermography mechanical vibrations with frequency ranging from 5-10 kHz are induced by an ultrasonic generator to travel through the specimen homogeneously causing the sample to vibrate in unison. Defect detection is based on the fact that areas defect faces will not movie in unison and the friction movement between the two faces will convert the vibrational energy to heat energy. The heat generated between the surfaces will be conducted to the surface through conduction and an IR camera will be used to monitor the change in temperature on the surface. The defect detection is also influenced by increasing or decreasing the mechanical excitation frequency. Vibrothermography has been used to detect closed cracks in metals and ceramics as well as delamination in composite materials [29].

1.5 Thesis Objective

The main objective of this study is to analyze various approaches and heating configurations for defect detection for in-pile measurement in the reactor environment and for laboratory environments at either room or elevated temperatures. A crack model has been developed and four different configurations have been considered for defect detection: -

1. Uniform volumetric heating within solid and imaging using optical IR fiber bundles to simulate defect detection for in-pile measurement in reactor environment. (Steady State condition)
2. Uniform volumetric heating within solid and a frequency modulated surface heating using optical fiber bundles to simulate defect detection for in-pile measurement in the reactor environment. (Lock-in Thermography (LIT), Transient)
3. Surface Heating on the solid (Uniform/Gaussian heating) for defect detection under laboratory environments. (Steady State condition)
4. Frequency modulated heating on the top surface (Uniform/Gaussian heating) for defect detection under laboratory environments. (Lock-in Thermography (LIT), Transient)

An analysis for each of the heating configurations has been performed to identify the optimal configuration. One of the unique aspects of the modeling is inclusion of noise/smearing due to thermal sensitivity and spatial resolution of IR camera. The noise in the image is introduced due to the detectors, sensors, signal processing system and the electronic circuit. Additionally the optical system introduces optical diffraction (Fraunhofer diffraction) or smearing and an optical aberration, which introduce non linearities and limit the image spatial resolution to a great extent. Note that for volumetric heating configurations, optical IR fiber bundles and the harsh reactor environment surrounding fuel rods induce additional noise/distortion.

This research was performed under In-Pile Instrumentation program supported by Department of Energy, Office of Nuclear Energy.

Chapter 2: INFRARED THERMAL MODELLING

2.1 Introduction

The entire infrared image modelling process can be divided into infrared thermal modelling and infrared sensor modelling [30]. The complete infrared image modelling process block diagram is shown in Figure 12. The modelling process has been proposed on basis of different configurations for defect detection.

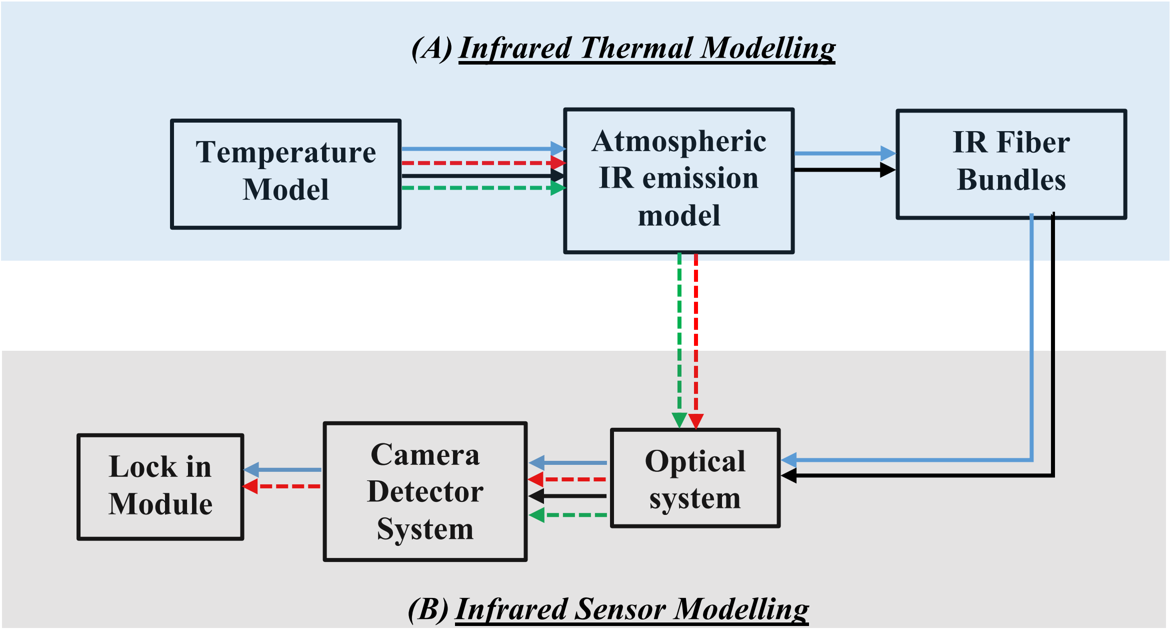

Figure 12: Infrared image modelling block diagram

The modelling process pertaining to the different configurations are: -

1. Volumetric heating within the solid and imaging using IR fiber bundles under reactor environment (Steady State): - Solid Black (━━)
2. Uniform Volumetric heating and frequency modulated heating on surface using optical IR bundles under reactor environment (LIT, transient): - Solid Blue (━━)
3. Uniform surface heating under laboratory conditions (Steady State): - Dashed Green (-----)
4. Frequency modulated uniform heating on the top surface under laboratory conditions (Lock-in Thermography (LIT), Transient): - Dashed Red (-----)

As seen in Figure 12, the infrared thermal modelling comprises of the temperature model, atmospheric IR emission model and the IR fiber bundle modelling. The temperature model takes into account the heat diffusion governing equations and boundary conditions for the heating configuration and returns the temperature profile, which is used by the atmospheric IR emission model. The IR emission model is used for the radiation modelling and accounts for parameters such as working wavelength, emissivity, transmissivity etc. The IR fiber bundle model accounts for the attenuation and dispersion introduced due to the phenomena such as Rayleigh scattering, Mie Scattering, Intermodal Dispersion, Chromatic Dispersion etc [31]. A detailed discussion on the temperature model, atmospheric IR emission model and the optical fiber bundle modelling is presented in the following sections.

2.2 Temperature Model

The governing equation for a thermal model is defined by the general equation for heat transfer: -

$$\rho C \frac{\partial T}{\partial t} = \vec{\nabla}.(k\,\vec{\nabla}T) + \dot{Q} \tag{1}$$

The properties ρ, C, k represent the material density, specific heat and thermal conductivity respectively and are assumed to be independent of temperature. $\mathrm{T(x, y, z, t)}$ represents the temperature variable in terms of the three spatial variables $\mathrm{(x, y, z)}$ and time t. $\dot{\mathrm{Q}}$ represents the volumetric internal heating source and $\vec{\nabla}$ is the gradient operator. The equation (1) can be rewritten as shown below: -

$$\nabla^2 \mathrm{T} + \frac{\dot{\mathrm{Q}}}{\mathrm{k}} = \frac{1}{\alpha}\frac{\partial \mathrm{T}}{\partial \mathrm{t}} \tag{2}$$

Here ∇^2 is the Laplace operator and α, $\left(\alpha = \frac{\mathrm{k}}{\rho \mathrm{C}}\right)$, represents the thermal diffusivity of the material. The thermal diffusion governing equation for steady state models is reduced to: -

$$\nabla^2 \mathrm{T} + \frac{\dot{\mathrm{Q}}}{\mathrm{k}} = 0 \tag{3}$$

Equation (2) represents the general equation of heat transfer in the time domain. However, an equation in the frequency domain needs to be considered for thermal models involving harmonically modulated heat sources as in the case for Lock-in thermography. Performing a Fourier transform, Equation (2) transforms to: -

$$\nabla^2 \mathrm{T}_\omega = \frac{\mathrm{i}\omega \mathrm{T}_\omega}{\alpha} \tag{4}$$

Equations (3) and (4) are the governing equations for the thermal models involving steady state heating and harmonically modulated heating, respectively. The boundary conditions for the different heating configurations are defined in Table 1. The appropriate heating boundary conditions are implemented for each of the heating configurations. Additionally, convection boundary conditions are applied on all the adjacent walls and surfaces. Some important notes and results regarding the thermal model are presented: -

Table 1: Governing equations and boundary conditions for different heating configurations

Heating Configuration	**Boundary Condition (DC) component**	**Boundary Condition (AC) component**	**Governing Equation**
A. Uniform heating within solid, imaging with IR fiber bundle (Steady State, Reactor Envmt.)	$q'' = h(T - T_0)$ all surfaces	---------	$\nabla^2 T + \frac{\dot{Q}}{k} = 0$
B. Uniform heating within solid and freq. mod. heat with fiber bundles (Lock in, Reactor Envmt)	$q'' = Q_0$ top surface $q'' = h(T - T_0)$other surfaces	$q''_\omega = Q_0$ top surface $q''_\omega = 0$ other surfaces	$\nabla^2 T_\omega + \frac{\dot{Q}}{k} = \frac{i\omega T_\omega}{\alpha}$
C. Uniform surface heating (Steady State, Laboratory Envmt)	$q'' = Q_0$ top surface $q'' = h(T - T_0)$other surfaces	----------	$\nabla^2 T = 0$
D. Frequency modulated uniform surface heating (Lock in, Laboratory Envmt)	$q'' = Q_0$ top surface $q'' = h(T - T_0)$other surfaces	$q''_\omega = Q_0$ top surface $q''_\omega = 0$ other surfaces	$\nabla^2 T_\omega = \frac{i\omega T_\omega}{\alpha}$

1. While performing thermal modelling for cracked geometries, the cracks have an insulation boundary condition as they do not conduct heat [11].

2. For steady state heating configurations (A) and (C) as described in Table 1 (Section 2.2), the temperature output by the thermal model comprises of only the DC component. This can be attributed to the fact that heating configurations (A) and (C) consist of only DC component boundary conditions and are void of any AC component boundary conditions.
3. For lock in heating configurations (B) and (D) as described in Table 1 (Section 2.2), the temperature output by the thermal model is a sum of the DC and AC component. This is because heating configurations with frequency modulated heating have a DC and AC boundary condition.

$$T_{\text{lock-in}} = T_{DC} + T_{AC} \tag{5}$$

Consider a frequency modulated surface heating of: $P = [0.1 + 0.05 \times \sin(\pi\, f_o t)]$ W with $f = 0.1$ Hz, on a crack model (cylinder with a longitudinal through crack) as shown in Figure 13.

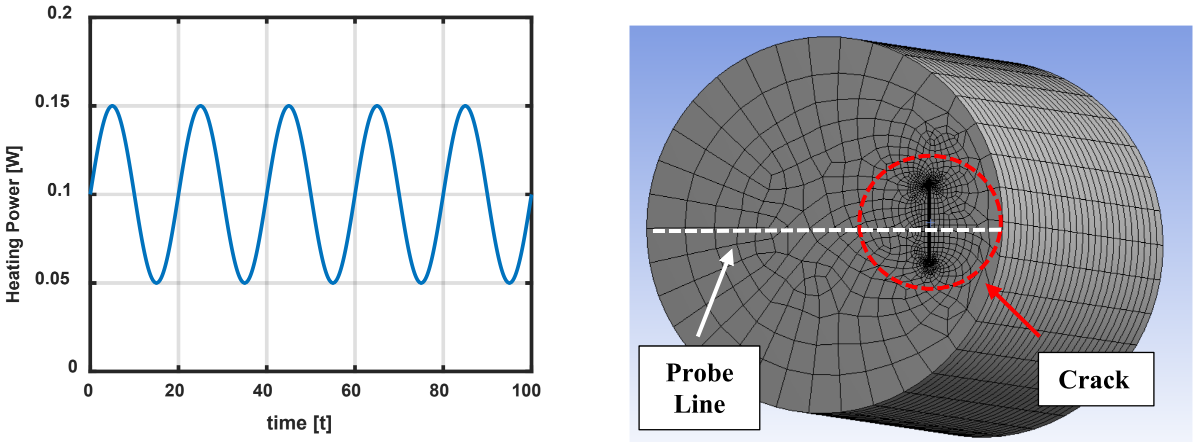

Figure 13: Temperature modelling for Lock in Thermography: - Frequency modulated surface heating profile (left), Simulation Mesh used in the Finite Element Model (right)

The model material is considered as Uranium di Oxide [32] with material properties and the model/crack dimensions summarized in Table 2.

Table 2: Material Properties of $\mathrm{UO_2}$ at T = $350\ K$ and Model/Crack Dimensions

Material Property ($\mathrm{UO_2}$) [32]	**Model Dimensions (Cylinder)**	**Crack Dimensions (longitudinal through crack)**
$\mathrm{k = 6.2\,\frac{W}{mK}}$	Diameter = 1 cm	Crack length = 0.2 cm
$\mathrm{\rho = 10970\,\frac{kg}{m^3}}$	Thickness = 1 cm	Crack width = 0.01 cm
$\mathrm{c = 258\,\frac{J}{kg.K}}$		Distance from center = 3.5 cm

The temperature contour plot for the top surface and the plot for the probe line are shown in Figure 14. Note that the physical thermal properties ρ, C, k are assumed to temperature independent. Considering an ambient temperature of 300K, the overall temperature profile attains a maximum temperature of 342.86 K. The crack is clearly visible in the temperature line plot and highlighted in red. The DC and AC temperature line plot components are shown in Figure 15. The DC temperature and AC temperature (Amplitude) components attain maximum values of 342.84 K and 1.34 K respectively.

4. Different forms of surface heating can be considered to heat the sample. The most readily forms of surface heating are uniform surface heating (achieved using halogen lamps) and gaussian heating profile (achieved using point laser).

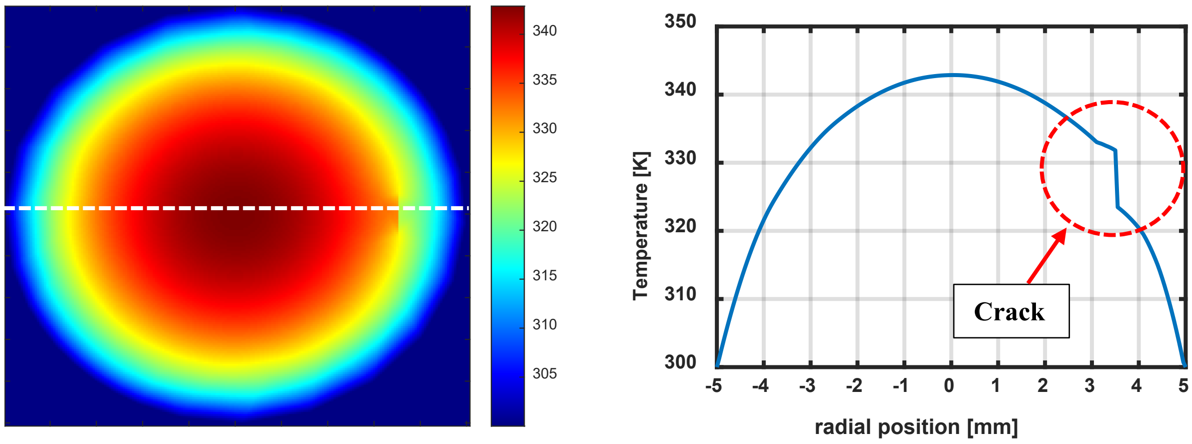

(A) (B)

Figure 14: Temperature modelling for Lock in Thermography, $T_B = 300K$, (A) Temperature contour plot, (B) Temperature line plot for probe line

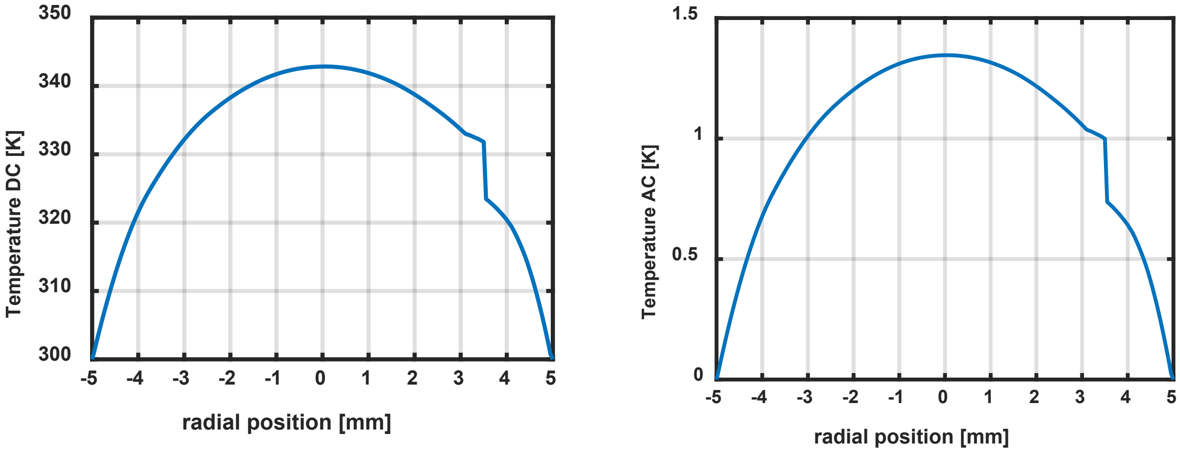

(A) (B)

Figure 15: Temperature modelling for Lock in Thermography (A) DC Temperature Component (B) Amplitude of AC Temperature Component for frequency modulated heat profile

The choice of the most optimum surface heating depends on the magnitude of temperature drop (ΔT) and the local temperature (T_{local}) around the crack. This is because the strength of infrared signal is directly proportional to the temperature magnitude. The two heating conditions have been modelled to identify the most optimal form of heating. A crack model has been developed on a fuel rod (represented as a cylinder) with longitudinal through cracks located at a distance of 1 mm, 2 mm, 3 mm and 4 mm from the center. The model, gaussian/uniform heating profiles are shown in Figure 16. The magnitude of the uniform heating profile is equal to the average of the gaussian profile.

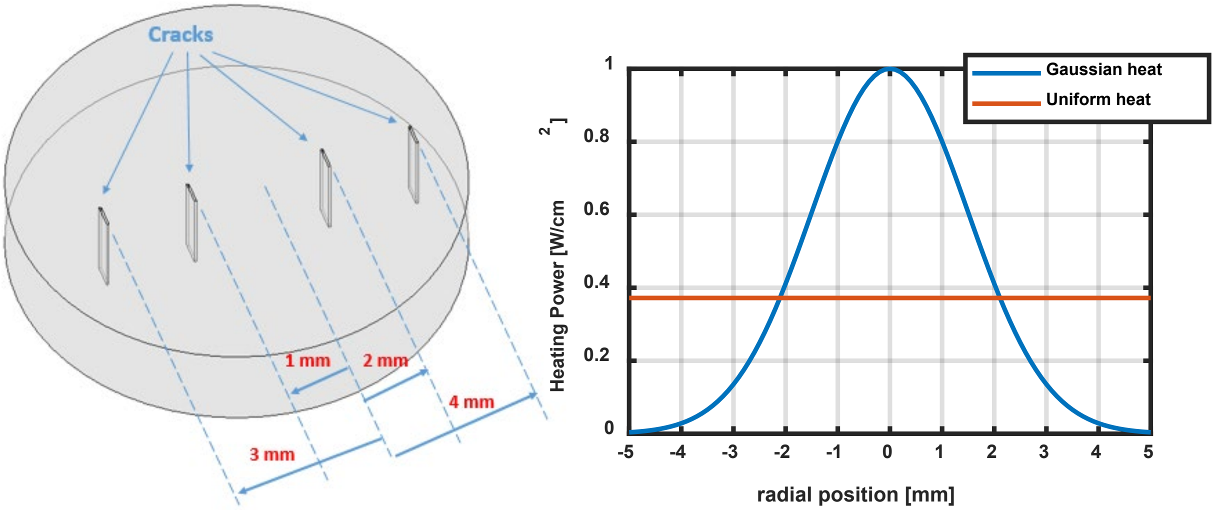

Figure 16: Surface heat finite element modelling: - Simulation Mesh used in the Finite Element Model (left), Gaussian/Uniform Heating Profiles (right)

Comparison of the temperature profile for the temperature profile generated by the Gaussian and uniform heating profile is shown in Figure 17. The temperature line plot has been generated for the line profile (y = 0) passing through the center of the four longitudinal cracks. Moreover the quantitative values of ΔT and T_{local} for Uniform and Gaussian heating conditions are summarized in Table 3. Observing Figure 17 and Table 3 the following observations can be made: -

- For radial positions 1 mm, 2 mm and 3 mm the ΔT for Gaussian heating is greater than the ΔT for uniform heating. Only for radial position 4mm the ΔT for Uniform heating is greater than the ΔT for Gaussian heating.
- Additionally for radial positions 2 mm, 3 mm, 4mm the T_{local} for Uniform heating is greater than the T_{local} for Gaussian heating. Only for radial position 1 mm the T_{local} for Gaussian heating is greater than the T_{local} for Uniform heating.
- Overall while the Gaussian heating profiles induce a greater ΔT across the crack, it generates a much lower T_{local} as compared to the Uniform heating profile.

Note that the choice of heating configurations (Uniform/Gaussian) depends on the IR camera parameters, crack geometry, material properties, governing/boundary conditions etc. The infrared camera modelling and parameters are discussed in Section 3.2.

Table 3: ΔT and T_{local} for Uniform and Gaussian heating conditions

	r = 1 mm	r = 2 mm	r = 3 mm	r = 4 mm
ΔT (Gaussian)	34.57 K	45.64 K	38.37 K	27.85 K
ΔT (Uniform)	9.01 K	17.84 K	27.60 K	39.44 K
T_{local} (Gaussian)	535.64 K	456.01 K	375.46 K	316.14 K
T_{local} (Uniform)	493.10 K	470.17 K	429.71 K	372.46 K

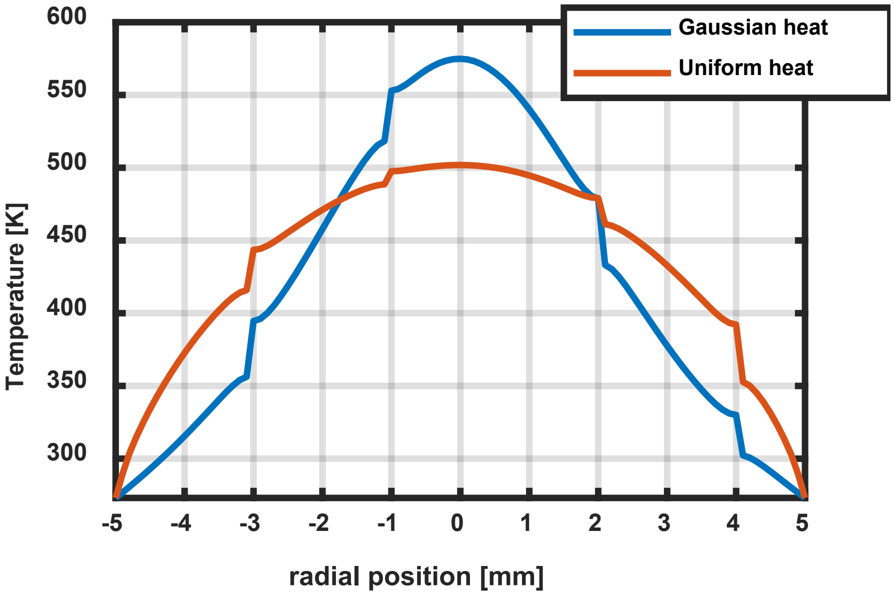

Figure 17: Thermal profile for Gaussian and Uniform Heating

2.3 Atmospheric IR emission model

2.3.1 IR emission modelling

Atmospheric infrared radiation is the radiation emitted by the surface of an object having a temperature above absolute zero. The spectral emissive power for a black body, or the rate at which the radiation is emitted per unit area in all possible directions for a particular wavelength λ is: -

$$E_{\lambda,b}(\lambda, T) = \frac{c_1}{\lambda^5\left(\exp\left(\frac{c_2}{\lambda T}\right)-1\right)} \tag{6}$$

The higher the temperature of the surface, greater the intensity of the emitted infrared radiation. Figure 18 shows the distribution of radiation emitted by a blackbody at different temperatures and wavelength [33]. As can be seen, the peak of the curve for a hotter object is larger. In addition, there is an inverse relation between the temperature and the wavelength of the peak of the emission. This relation is termed as the Wein's law which is given as:

$$\lambda_{\text{peak}} = \frac{0.0029}{\text{T (K)}}\ \mu\text{m} \tag{7}$$

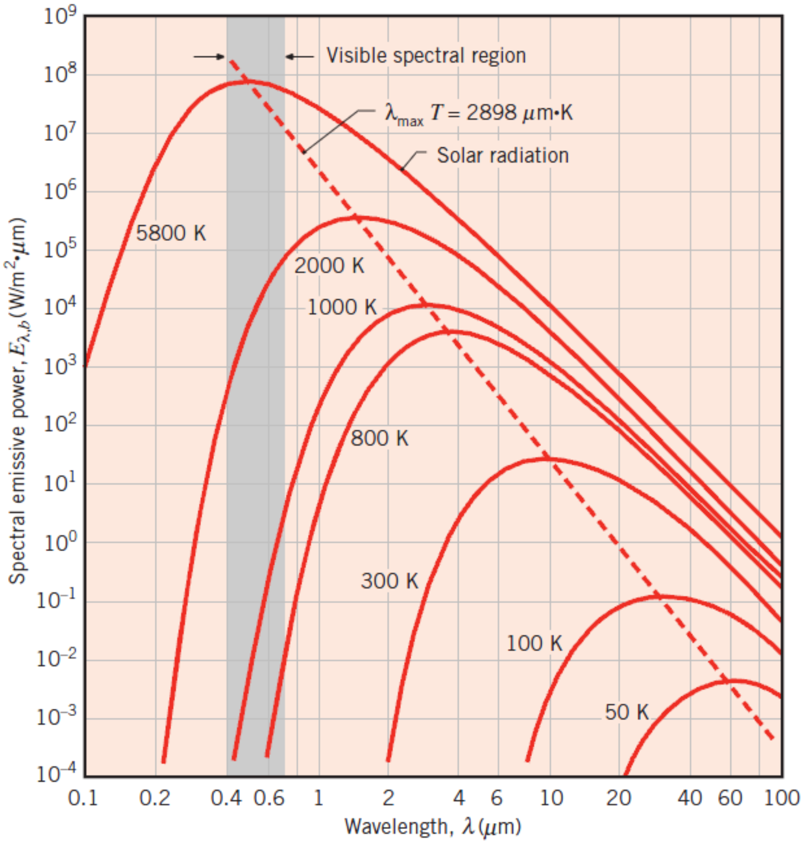

Figure 18: Spectral blackbody emissive power [33]

Hence depending on the temperature of the object, the choice of camera and camera wavelength must be made to maximize the IR radiation intensity. An additional factor affecting the IR radiations as it passes through the atmosphere is the atmospheric transmittance, $\tau_{\text{atm}}(\text{T})$. Infrared radiation travels through air, being absorbed by various air particles, mostly by CO_2 and H_2O [34]. The degree to which air absorbs infrared radiation depends on the wavelength. Figure 20 shows the atmospheric transmittance for different wavelengths [35] at one nautical mile, 15.5^0 C, 70% relative humidity and at sea level.

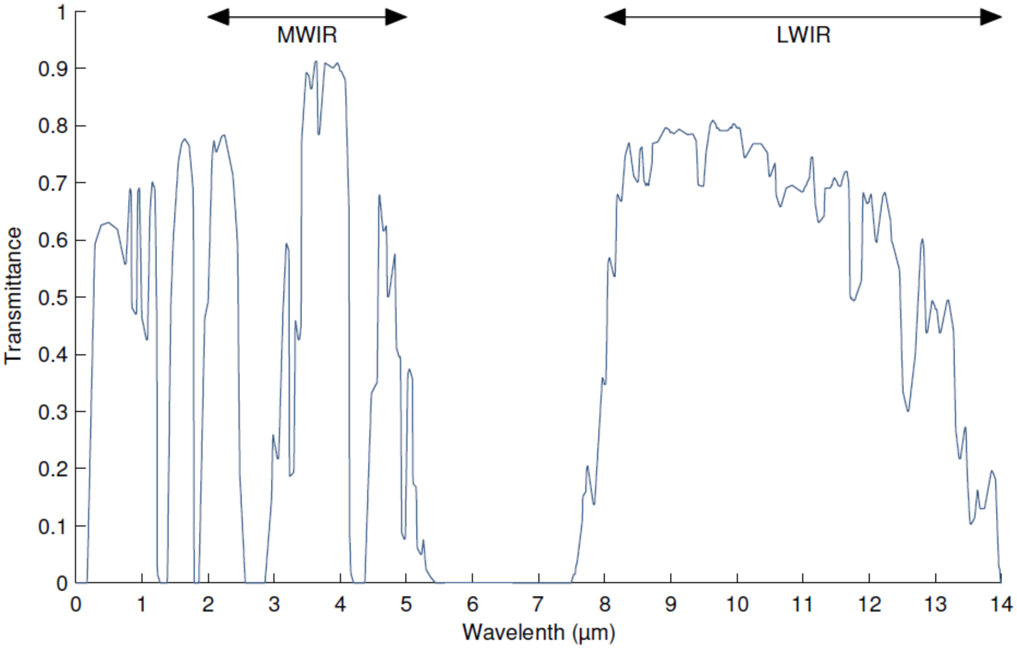

Figure 19: Atmospheric transmittance for wavelength range (0 – 14 µm) [35]

As seen in Figure 19, from 0.4 µm to 0.7 µm, only 60% of the emitted radiation is transmitted. However, between 5 µm and 7.5 µm, almost no radiation is transmitted. The atmosphere absorbs all of this radiation. Therefore depending upon transmittance at different wavelength, infrared measuring devices use either SWIR (0.9 µm to 1.7 µm), MWIR (2 µm to 5 µm) or LWIR ranges (7 µm to 13 µm). Additionally it is important to note that the under realistic conditions the specimen will not be a perfect blackbody and have a certain value of emissivity $\varepsilon(\lambda, \mathrm{T})$ associated to it. Hence overall the atmospheric IR radiation emitted a point of area A_n on the surface of the specimen and received by the IR camera is given as: -

$$\mathrm{E}(\lambda, \mathrm{T}) = \int_{\lambda_1}^{\lambda_2} \left(\frac{c_1}{\lambda^5 \left(\exp\left(\frac{c_2}{\lambda \mathrm{T}}\right) - 1 \right)} \times \varepsilon(\lambda, \mathrm{T}) \times \tau_{atm}(\lambda, \mathrm{T}) \right) d\lambda \times A_n \cos\emptyset \times \omega \tag{8}$$

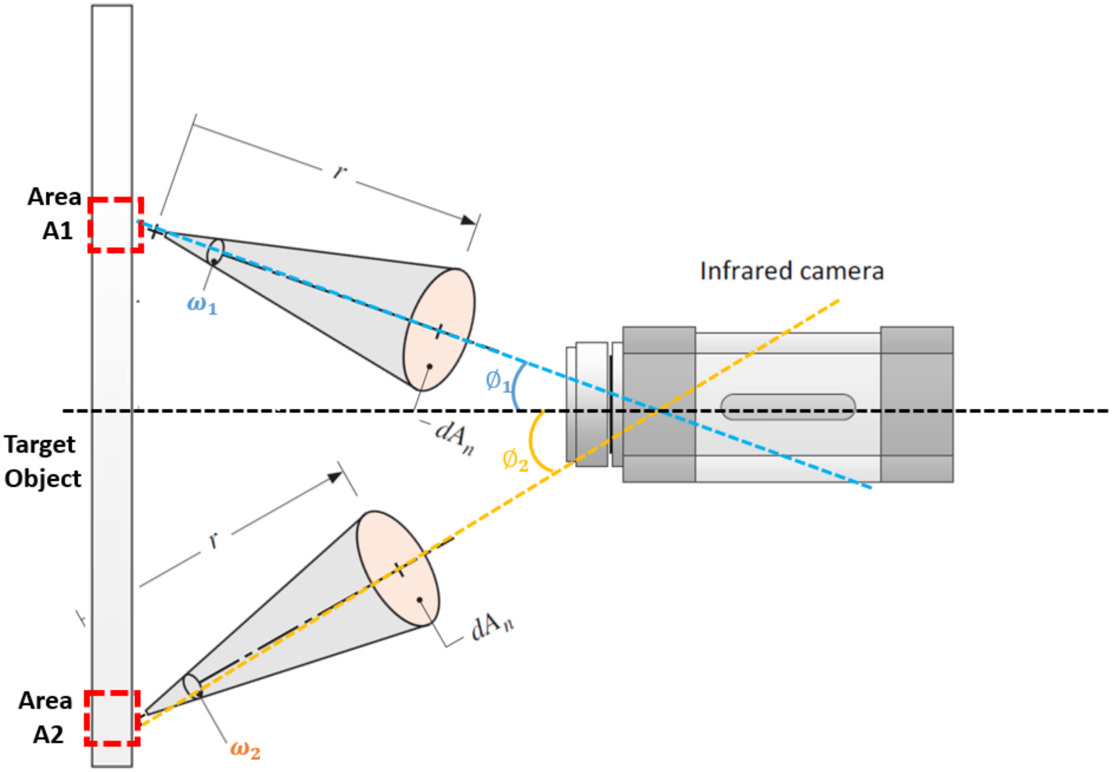

Figure 20: Atmospheric IR emission model [35]

Figure 20 illustrates the atmospheric IR emission model [35]. Here the atmospheric IR radiation received by the IR camera has been calculated for an area A_1 on the target object having a temperature T with surface emissivity $\varepsilon(\lambda, \mathrm{T})$. The atmospheric transmittance is considered as

τ_{atm}, solid angle and the inclination between the camera and the target object are ω and $\emptyset$ respectively. The IR emission here has been calculated for a wavelength range from λ_1 to λ_2 respectively.

2.3.2 Emissive Power IR Modelling

Considering the temperature line plot shown in Figure 14(B) (Section 2.2), the corresponding emissive power profiles, $E_b(T)$ (rate at which the radiation is emitted per unit area in all possible directions) have been plotted by considered the crack model as a perfect black body ($\varepsilon = 1$).

$$E_b(T) = \int_{\lambda_1}^{\lambda_2} \frac{c_1}{\lambda^5\left(\exp\left(\frac{c_2}{\lambda T}\right)-1\right)} d\lambda$$

The irradiance profiles have been constructed for wavelength ranges of, 0.9 – 1.7 µm, (SWIR), 2 – 5 µm, (MWIR) and 7 – 13 µm, (LWIR). As observed from Figure 21, for $T_b = 300\,K$, the emissive power (E_b) for the LWIR range > E_b for MWIR range > E_b for SWIR range. However as observed from Figure 22, for $T_b = 600\ K$, the emissive power (E_b) for the MWIR range > E_b for LWIR range > E_b for SWIR range. This correlation can also be understood from the Weins law (7). Note that the emissive power is one of the important factors which governs the choice of IR camera for a given heating configuration. It should be noted that while the intensity of the radiation in the SWIR range is lower over the 300 – 600 K temperature range, the SWIR camera has much lower noise (noise equivalent power, noise equivalent temperature difference) as compared to the MWIR and the LWIR camera. Hence the choice of the IR camera is not made on the sole basis of the Emissive Power. This shall be discussed in detail in the Section 3.1.7.

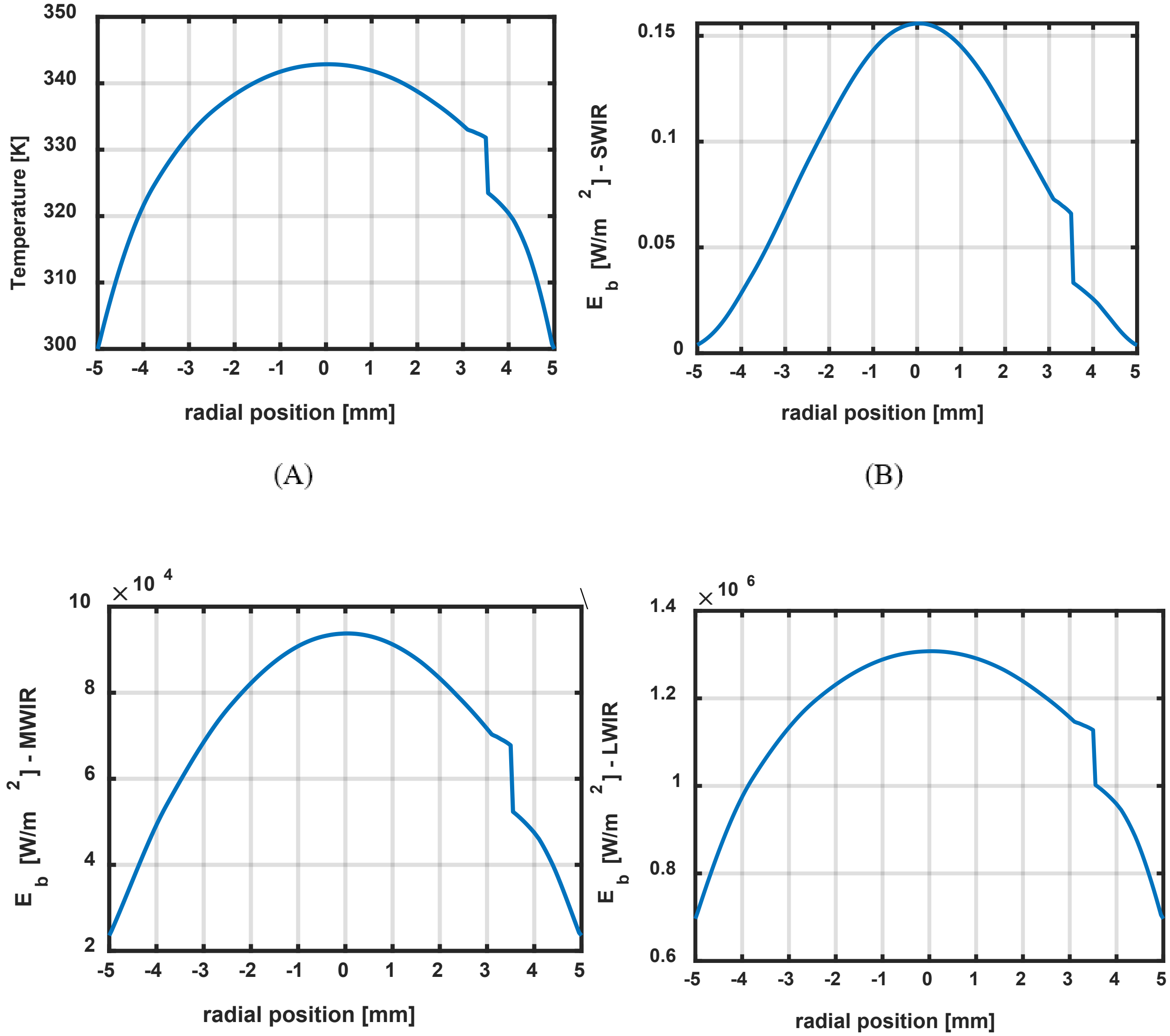

(A) (B)

(C) (D)

Figure 21: Comparing emissive power response for different wavelength ranges, ($T_b = 300$ K) (A) Temperature line plot, (B) Emissive Power for SWIR range (0.9 – 1.7 µm) (C) Emissive Power for MWIR range (2 – 5 µm), (D) Emissive Power for LWIR range (7 – 13 µm)

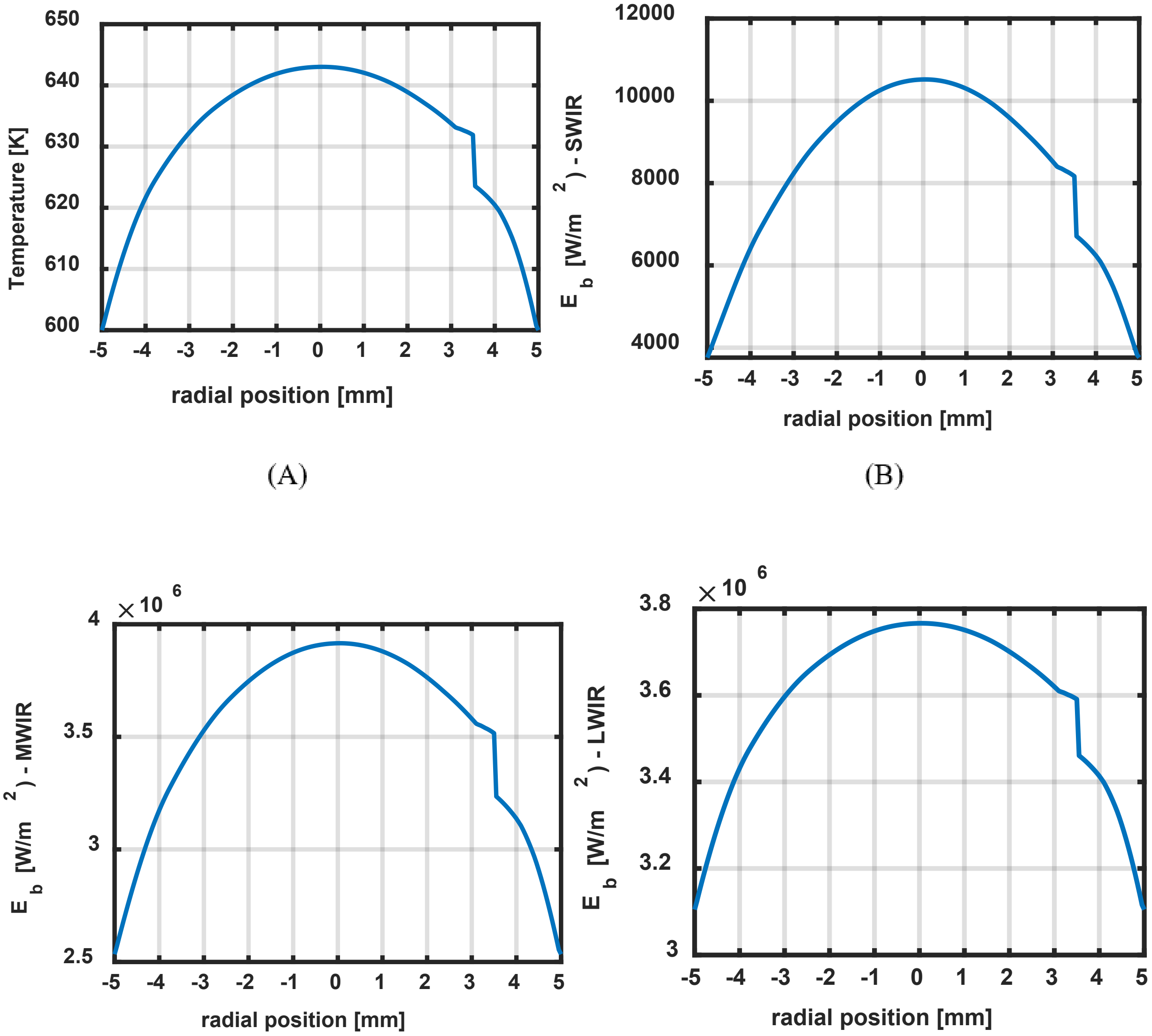

(A) (B)

(C) (D)

Figure 22: Comparing emissive power response for different wavelength ranges, (T_b = 600 K) (A) Temperature line plot, (B) Emissive Power for SWIR range (0.9 – 1.7 µm) (C) Emissive Power for MWIR range (2 – 5 µm), (D) Emissive Power for LWIR range (7 – 13 µm)

2.4 Optical fiber bundle modelling

The harsh environment inside of a nuclear fuel reactor poses challenges for measurement and instrumentation using traditional instrumentation (thermocouples, strain gauges, etc.). Such instruments are not well suited for extended operation in such a harsh environment. IR Optical fiber bundles offer a potential to be used for instrumentation in high temperature irradiation experiments [36].

Optical fibers can be defined as medium to transport optical energy and information. They have a central core surrounded by a concentric cladding with slightly lower refractive index. Since the core has a higher index of refraction than the cladding, light will be confined to the core if the angular condition for total internal reflectance is met. The total internal reflection is the basic principle through which the optical signal/information is transmitted through the optical fiber bundles.

The optical IR fiber bundles are targeted primarily for providing high spatial resolution infrared images of nuclear fuel rods inside the fuel reactor which operate in harsh conditions and which are inaccessible to the infrared camera. Some of the goals for achieving in reactor fuel cracking using optical fiber bundles include identifying suitable fiber optic material and parameters for achieving maximum signal transmission and minimizing the signal dispersion.

Figure 23 shows a classification of fiber types by structure [31]: solid-core fibers, hollow waveguides, and micro-structured fibers. Commercially available infrared optical fibers are made of different core materials like zirconium fluoride (ZrF4), indium fluoride (InF3), Chalcogenide (CIR) and Polycrystalline fiber bundles, each having high transmittance over different spectral ranges.

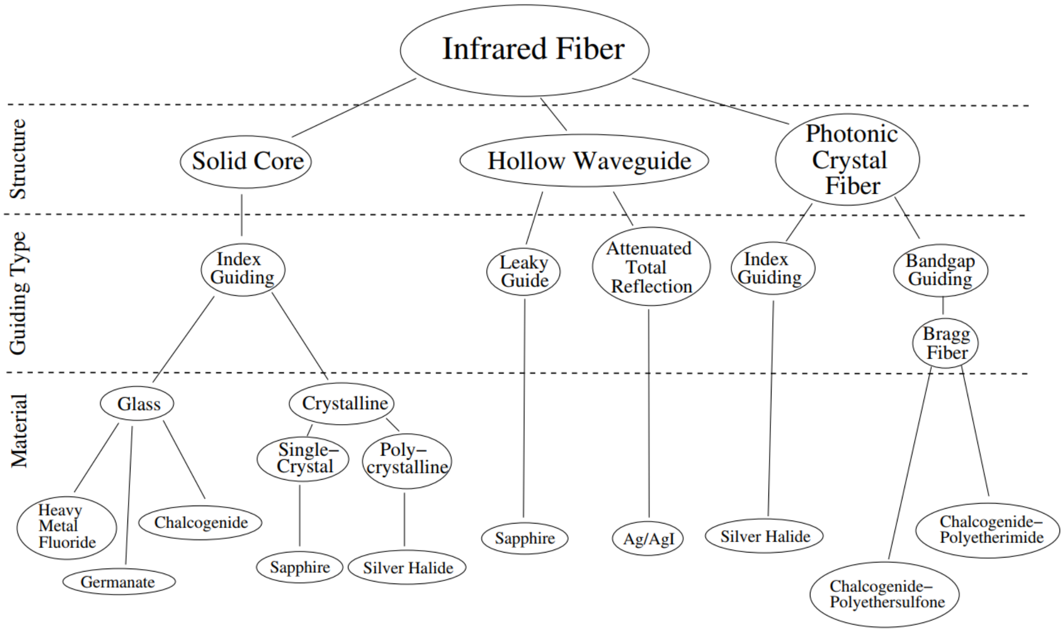

Figure 23: Classification of infrared fibers [31]

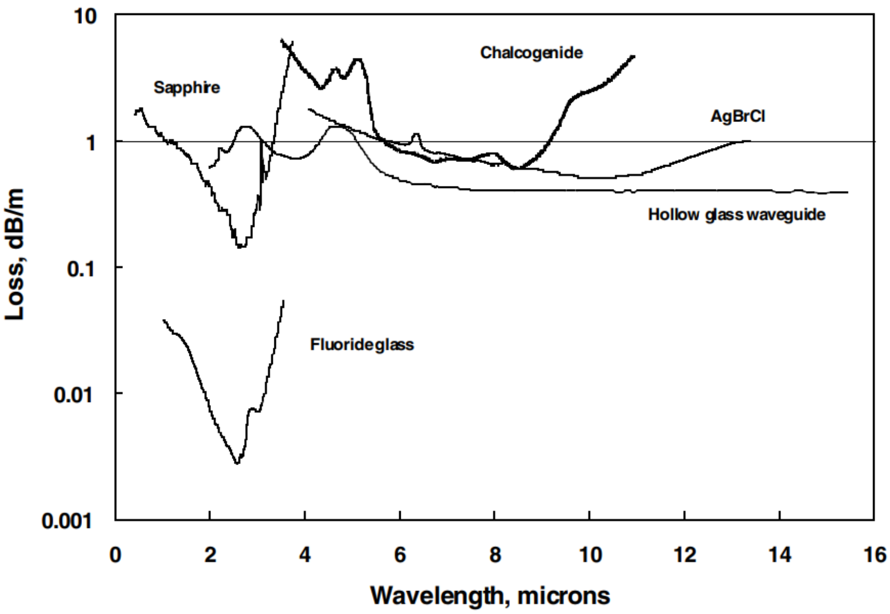

Figure 24: Composite loss spectra for some common IR fiber optics: fluoride glass, sapphire, chalcogenide glass, AgBrCl, and hollow glass waveguide [37]

Figure 24 gives the loss (dB/m) values for some of the most common IR fibers [37]. The IR fiber losses is termed as attenuation and is defined as the amount of light lost between the input and the output. Fluoride fibers show the lowest attenuation of all fibers transmitting in the mid infrared range. The expression for attenuation is given as: -

$$\mathrm{T} = \frac{\mathrm{P_{out}}}{\mathrm{P_{in}}} = (\mathrm{Pf})(1 - \mathrm{R}^2)\mathrm{e}^{-\alpha L} \qquad (9)$$

Here T is the Transmittance, $\mathrm{P_{Out}}$, $\mathrm{P_{in}}$ are the input and output power respectively, Pf is the packing fraction, R is the reflection coefficient, L is the fiber length and α is the fiber attenuation coefficient. Packing factor is defined as the ratio of the core area to the total area in the cross section of the fiber. Moreover reflection coefficient losses originate when light is incident upon the surface of fiber bundles and a portion of the light gets reflected back instead of transmitting through the fiber bundle.

Attenuation in optical fibers originates due to a number of factors namely absorption losses, scattering losses (Rayleigh Scattering, Mie Scattering, Brilloun Scattering), Macrobending / Microbending losses, Packing factor losses etc [31]. Absorption losses account for the majority of the attenuation. Absorption is caused due to the materials of fiber optic which absorb some of the light power and transfer it into other forms of energy like heat, due to molecular resonance and wavelength impurities. In addition to the signal attenuation, dispersion form as the second limiting parameters for the use of optical fiber bundles for infrared imaging applications. Dispersion limits the spatial resolution of the signal and is caused due to intermodal dispersion, material dispersion, waveguide dispersion and polarization mode dispersion (only in single mode fibers) [38].

The dispersion introduced due to infrared optical bundles is characterized and modelled by the Modulation Transfer Function (MTF). The MTF function is a measurement of the ability of an optical system to transfer contrast at a particular resolution from the object to the image. It incorporates the resolution and the contrast into a single specification. Figure 25 shows the MTF of a sample core fiber bundle [39]. Here the X axis defines the spatial frequency or the lines per mm and the Y axis defines the ability of the system to transfer the contrast at the particular spatial frequency. Here it's understandable that as line spacing decreases (i.e. the frequency increases) on the target, it becomes increasingly difficult for the system to efficiently transfer this decrease in contrast; as result, MTF decreases. The MTF function for the fiber bundles is found experimentally using the knife edge method [40].

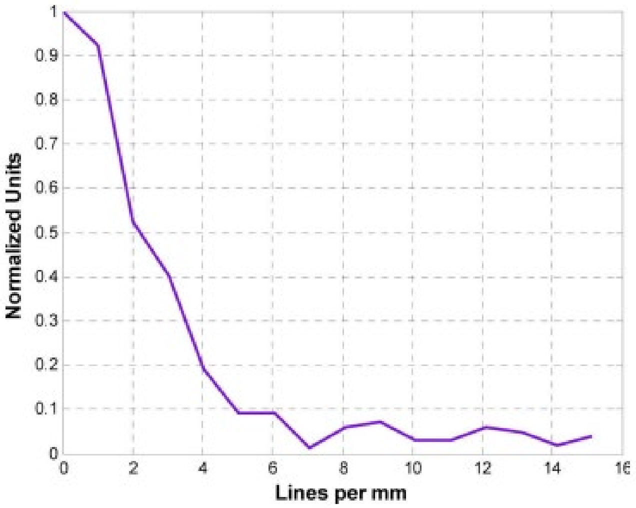

Figure 25: MTF of a 100 µm core fiber bundle [39]

Understanding that optical IR fiber bundles will be used for in-pile applications, the choice of materials should be such which can withstand high temperatures. Additionally a major limitation of using IR optical fibers under in-pile imaging with harsh environment, is the attenuation of the signal due to the effects of the temperature/irradiation. A number of computational and experimental studies have been conducted to study the effects of high dose and temperature radiation on IR optical fibers [36], [41], [42]. Figure 26 illustrates the added attenuation in sapphire optical fiber as it is heated over time (0 – 300 hrs) continuously to $1500^{0}C$. Over time sapphire shows reasonable amounts of attenuation from 0 to $900^{0}C$. However the attenuation in the sapphire fiber increase to unexpectedly high levels for temperatures over $1000^{0}C$. At such high temperatures, the fiber optic signal from a sensor can be easily lost due to high attenuation.

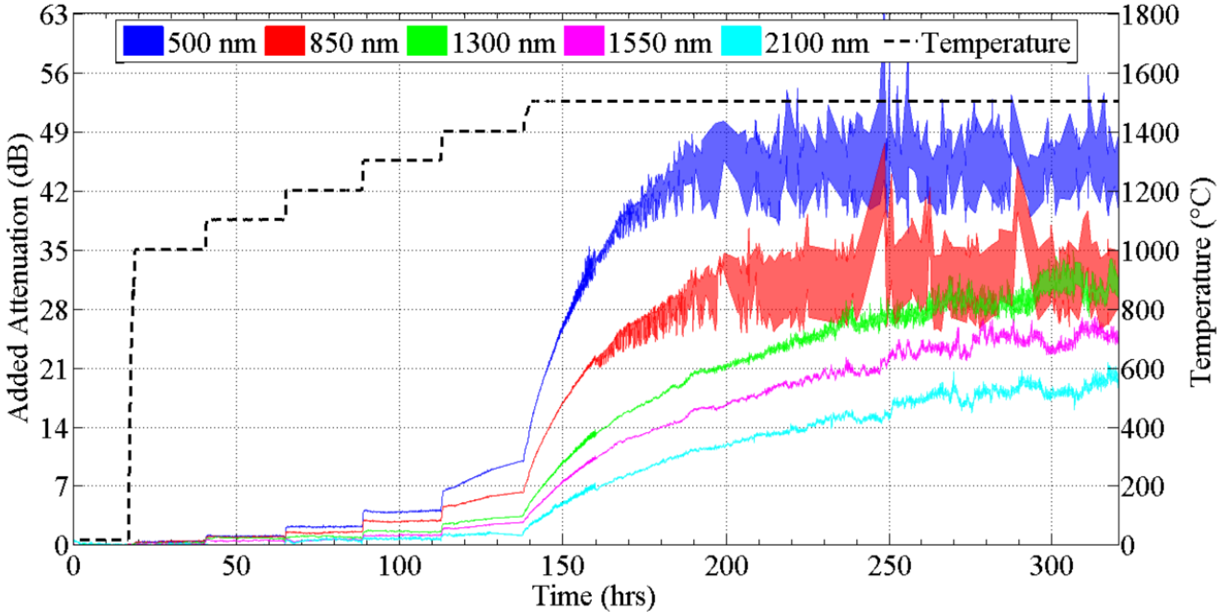

Figure 26: Graph depicting time (hours) vs added attenuation (dB) of multiple wavelengths (nm) of light propagating through sapphire optical fiber as it is heated continuously up to 1500 C [42]

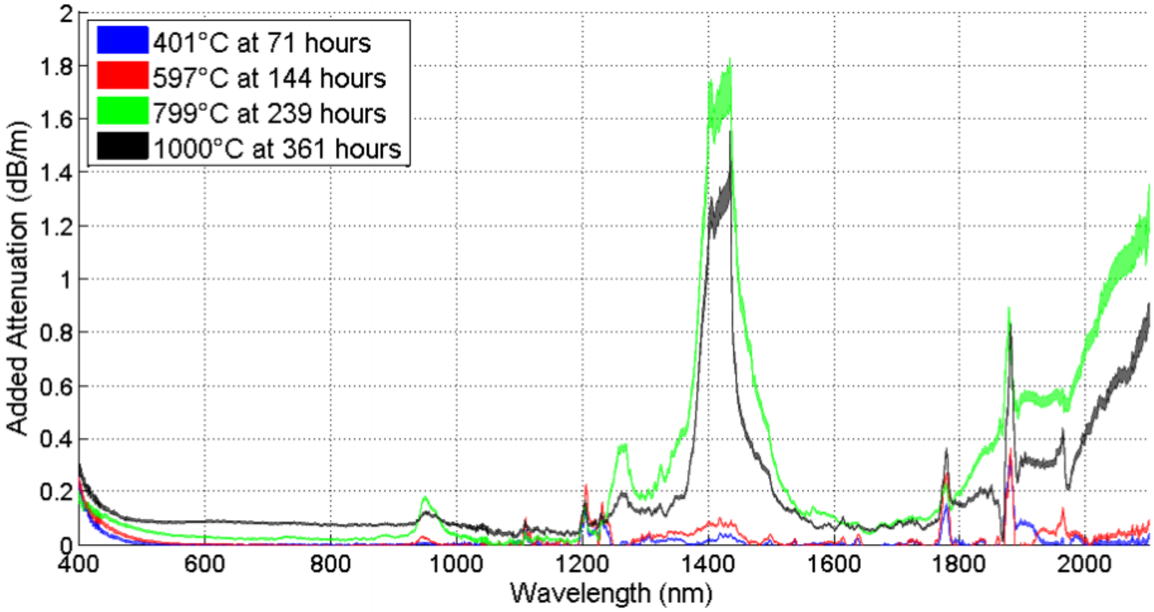

Figure 27: Graph depicting wavelength (nm) vs added attenuation (dB/m) of a SMF-28 silica optical fiber as it is heated continuously up to 1000^0C [42]

A similar plot has been shown in Figure 27 for a SMF-28 silica optical fiber. Here the attenuation value keeps on increasing with time as the optical fiber is continuously heated. It is important to note that Figure 26 and 27 illustrate only the influence of continuous heating on attenuation of sapphire/silica optical fibers. The radiation effects (gamnma rays and neutrons) from a nuclear reactor induce an added attenuation over time.

Chapter 3: INFRARED SENSOR MODELLING

The complete infrared image modelling is categorized into infrared thermal modelling and infrared sensor modelling [30] . The Infrared Sensor Modelling comprises of the Optical System, Camera Detector System and the Lock in Module. The optical system model is used for analyzing the smearing introduced in the signal due to optical diffraction. A study on diffraction limited optics has been performed and parameters such as the lens aperture diameter, focal length, f-number etc. have been considered [43]. The introduction of noise in the signal is performed in the camera detector model. Analysis on the noise introduced due to different types of IR cameras has been performed while accounting for factors such as Specific Detectivity, Noise Equivalent Power etc [44]. Next the lock in module block is used for fitting the input signal w.r.t a reference signal and returning the amplitude, phase profiles [45]. A detailed discussion on each of the blocks under infrared sensor modelling is presented in the following sections.

3.1 Infrared (IR) Camera Modelling

3.1.1 Schematic Block Diagram of the IR camera

The IR camera can be divided into five major subsystems namely: - optics and scanner, detector and detector electronics, digitization, image processing, and image reconstruction. A detailed block diagram for the IR camera [44] is shown in Figure 28. The optical system is the first part of the IR camera and is responsible for focusing the infrared radiation emitted from the target object onto the detector element. Commonly used materials for the optical lens include, Zinc Sulphide, Germanium, Zinc Sulphide, Silicon, Sapphire, quartz etc.

IR cameras use different techniques for projecting the IR radiation onto the detector namely: - line scanning system and staring array. Under the line scanning system, the optics sweeps the field-of-view and sequentially projects the signal on a single array of detectors, thereby generating a complete image of the scene. However under the staring array, there is no scanner, the output is instead provided by adjacent detectors in a matrix like pattern [46].

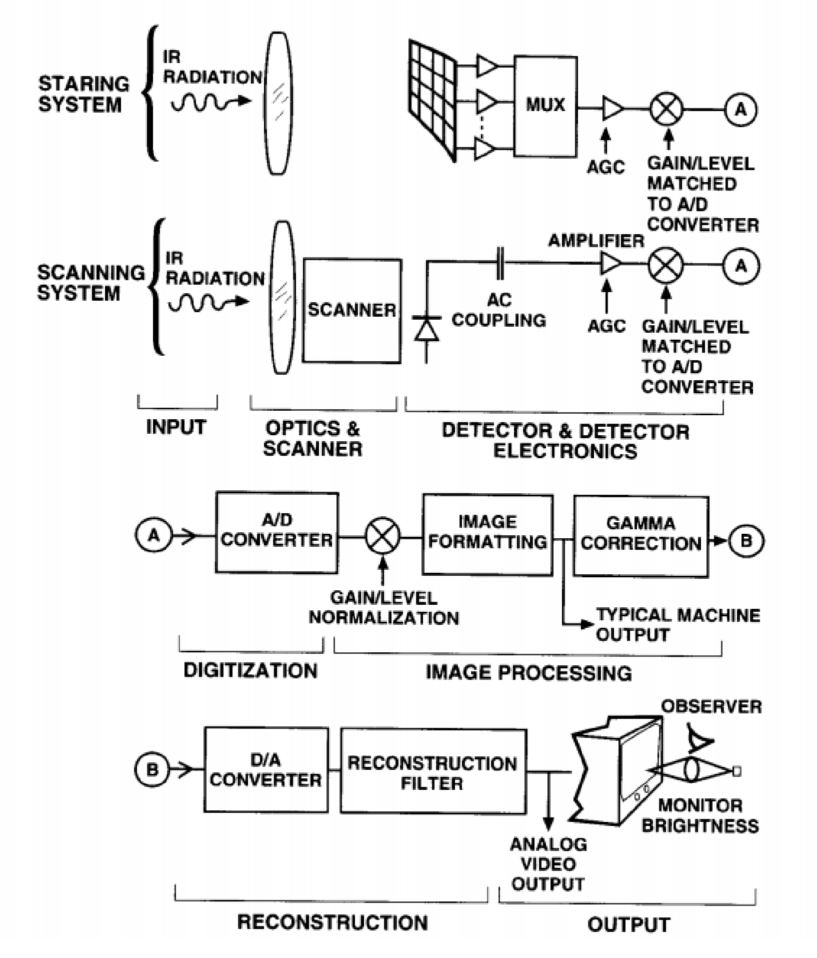

Figure 28: Block Diagram of an IR camera [44]

The IR camera detector consists of micrometer size pixels made of materials sensitive to IR wavelengths. These micrometer size pixels converts the projected infrared radiation into measurable electrical signal. The IR detectors can be classified as classical semi-conductors, novel semiconductors, and thermal detector. Commonly used detector materials include, Indium Gallium Arsenide (InGaAs) for SWIR detection, Indium antimonide (InSb) for MWIR detection, Mercury cadmium telluride (HgCdTe) for LWIR detection etc [44].

The signal from the detectors is sampled and digitized by the digitization subsystem to become easier to alter and process later on. The image processing and reconstruction subsystem can be used to enhance images, suppress noise, and smoothen out the signal to finally present an output video signal [47].

The radiation flux projected onto the IR camera detector is converted to an electronic signal as the radiation flux passes through different components of the IR camera. The camera output is given in terms of volts and is related to the input flux as: -

$$V_{\mathrm{detector}}(V) = \frac{A_D\,\tau_{\mathrm{optics}}}{4F^2} R_D M \tag{10}$$

Here V_{detector} is the camera output in volts, A_D is the active area of the detector, τ_{optics} is the transmittance of the optics, F is the F# number of the optical system, R_D is the responsivity (V/W) of the camera and M (W) is the radiation from the target or $E(\lambda, T)$ as defined in equation (8). The term $\left[\frac{T_{\mathrm{optics}}}{4F^2}\right]$ highlights the importance of the optical system in enhancing the detector output signal. Hence a high transmittance paired with a low F number of the optical system leads to a greater camera output. A summary of camera specifications for is presented in Table 4.

Table 4: IR Camera Specifications

	$\lambda_1 - \lambda_2$ µm	**Dynamic Range**	**NETD (mK)**	R_D **(A/W)**	**Detectivity** $\frac{(cm.)\sqrt{Hz}}{W}$	**NEP** $\frac{W}{\sqrt{Hz}}$	**Resolution** (Pixels)	**F#**	**Pitch**
SWIR (InGaAs)	0.9 – 1.7 µm	12 bit	>20	0.95	5×10^{12}	2×10^{-14}	640×512	1.3	15 µm
MWIR (InSb)	2 – 5 µm	14 bit	>20	0.0045	1×10^{9}	2×10^{-10}	640×512	2.3	15 µm
LWIR (ASi)	7 – 1.3 µm	14 bit	>50	0.0045	1×10^{9}	2×10^{-10}	1024×786	1.3	17 µm

The parameters Dynamic Range, NETD, Detectivity, NEP are resolution parameters which defines the performance of an IR system. They are discussed in detail in the following sections.

3.1.2 Performance parameter – Dynamic Range

The dynamic range is defined as the ratio between the largest and the smallest intensities that can be effectively imaged by the IR camera. In simpler terms dynamic range describes the ability of the IR camera to effectively transfer the contrast from the target to the image. An IR camera with a 12 bit and a 14 bit dynamic range can have a total of $2^{12} = 4096$ and $2^{14} = 16384$ discreet values respectively in its IR thermographic image. Hence the IR camera with the 14-bit dynamic range has a better capability of effectively transferring small resolution from the object to the IR image.

Figure 29 illustrates the radiation intensity plots for two imaging systems. The Intensity 1 and Intensity 2 plots have intensity bandwidth $(I_{max} - I_{min})$ values of $1.71 \times 10^{-8}\ W$ and $5.44 \times 10^{-9}\ W$ respectively. Moreover the Intensity drop (ΔI) across the crack in both signals is 6.27×10^{-10}W.

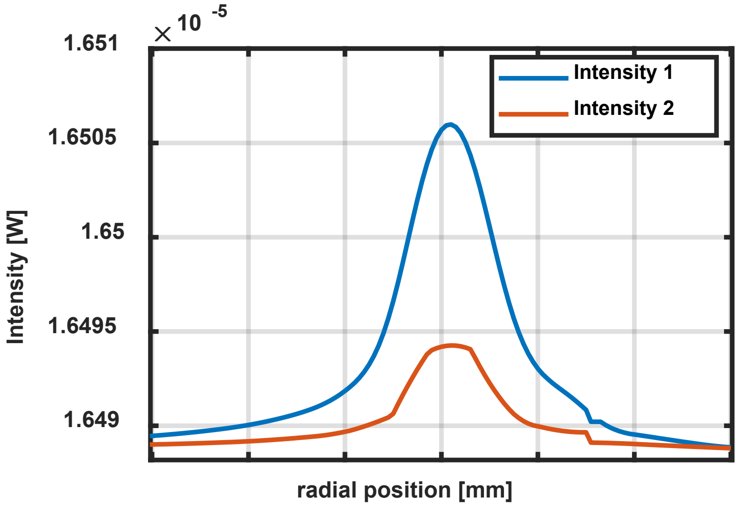

Figure 29: Radiation Intensity plots for two IR configurations

For the given values, the ratio of the intensity drop (ΔI) to the intensity bandwidth ($I_{max} - I_{min}$) is calculated for both the intensity plots. $\frac{\Delta I_1}{(I_{max}-I_{min})_1} = 0.03$, $\frac{\Delta I_2}{(I_{max}-I_{min})_2} = 0.12$. Comparing the two ratios, the magnitude of the crack signal has a much lower proportion as compared to the intensity bandwidth for the Intensity 1 profile. Hence if IR imaging were to be performed for the intensity profiles shown in Figure 29 the following recommendations can be made in terms of dynamic range: - The configuration corresponding to intensity 1 profile would need an IR camera with a high dynamic range to efficiently image the relatively small contrast in the crack signal. The configuration corresponding to intensity 2 profile has a greater magnitude of the crack signal in proportion to the intensity bandwidth. Hence an IR camera with a relative lower dynamic range would be able to efficiently image the relatively small contrast in the crack signal.

3.1.3 Performance parameters – Spatial Resolution

Ideally in an imaging system, the image for a point source should be a point source. However due to the nonlinearities and aberrations caused by the diffraction in the imaging system, the image is made of a core surrounded by concentric rings of diminishing intensity. The corresponding diffraction pattern is termed the Airy Disc with a diagram for the same shown in Figure 30 [43].

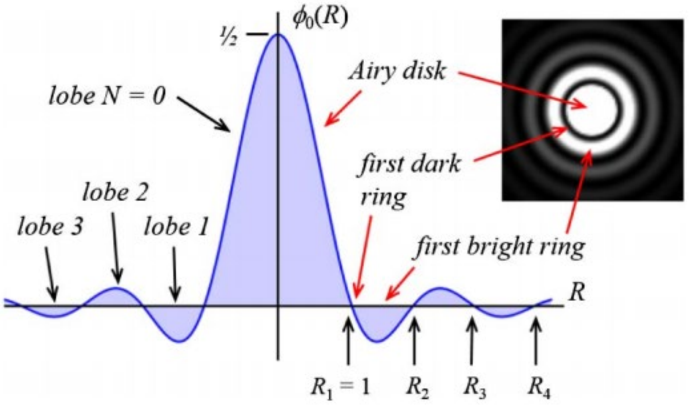

Figure 30: Airy's disk pattern introduced due to the optical system [43]

Here Δl is the spatial resolution, λ is the working wavelength. The characteristic equation for the Airy's disk is called the Point Spread Function. More generally PSF is the response equation of an imaging system to a point object. The PSF function is used for modelling the spatial resolution of an IR system. The PSF equation for an Airys disk is given as: -

$$\mathrm{PSF}_{\mathrm{Airys\ disk}} = \left[2\,\frac{\mathrm{J_1(r')}}{\mathrm{r'}}\right]^2 \tag{11}$$

Here $\mathrm{J_1}$ is the Bessel function of the first kind and $\mathrm{r'}$ is the normalized radius where, $\mathrm{r'} = \pi \mathrm{r}/\lambda \mathrm{f\#}$, r is the radial length under consideration, λ is the wavelength and f# is the f number. The MTF function as defined previously is an additional important parameter under spatial resolution modelling and can be defined as the ability of an imaging system to transfer contrast at a particular resolution from the object to the image. The PSF function is obtained by simply taking the Fast Fourier Transform (FFT) of the MTF function. The MTF introduced due to various components in the IR imaging system is shown in Figure 31 [30].

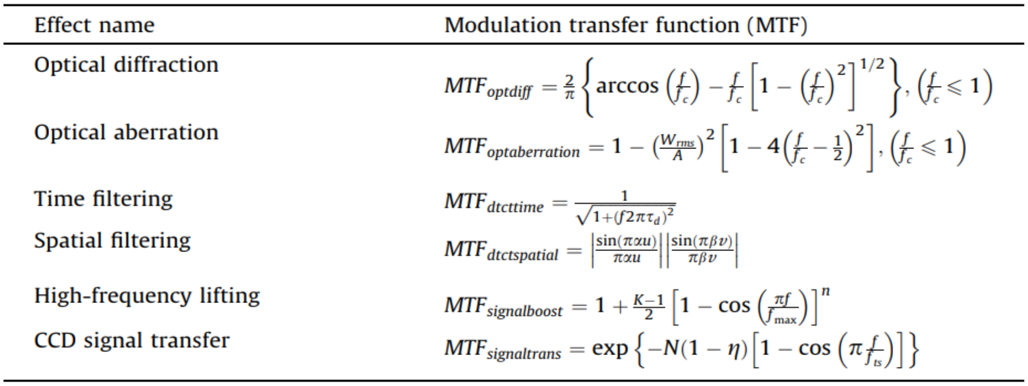

Effect name	Modulation transfer function (MTF)
Optical diffraction	$MTF_{optdiff} = \frac{2}{\pi}\left\{\arccos\left(\frac{f}{f_c}\right) - \frac{f}{f_c}\left[1 - \left(\frac{f}{f_c}\right)^2\right]^{1/2}\right\}, \left(\frac{f}{f_c} \leqslant 1\right)$
Optical aberration	$MTF_{optaberration} = 1 - \left(\frac{W_{rms}}{A}\right)^2\left[1 - 4\left(\frac{f}{f_c} - \frac{1}{2}\right)^2\right], \left(\frac{f}{f_c} \leqslant 1\right)$
Time filtering	$MTF_{dtcttime} = \frac{1}{\sqrt{1+(f2\pi\tau_d)^2}}$
Spatial filtering	$MTF_{dtctspatial} = \left\lvert\frac{\sin(\pi\alpha u)}{\pi\alpha u}\right\rvert\left\lvert\frac{\sin(\pi\beta v)}{\pi\beta v}\right\rvert$
High-frequency lifting	$MTF_{signalboost} = 1 + \frac{K-1}{2}\left[1 - \cos\left(\frac{\pi f}{f_{\max}}\right)\right]^n$
CCD signal transfer	$MTF_{signaltrans} = \exp\left\{-N(1-\eta)\left[1 - \cos\left(\pi\frac{f}{f_{ts}}\right)\right]\right\}$

Figure 31: MTF introduced due to different physical effects [30]

Now consider two optical systems operating in the MWIR region (2 – 5 µm). The first optical system has f# = 4.0 while the second optical system has f# = 2.3. Using the equation (12), the object space resolution for the two imaging systems has been calculated to be as: - $\Delta l_{\text{system 1}} = 34.16\mu m$ and $\Delta l_{\text{system 2}} = 17.08\mu m$. Since the object space resolution is proportional to the f#, a finer image resolution is obtained using the second imaging system. The corresponding graphical representation of the PSF functions for the two optical systems has been shown in Figure 32 (A). Considering a radiation input to the IR imaging system (Figure 32(B)), the spatial resolution modelling has been performed. Performing a convolution integral between the input radiation (M) and the two PSF functions, the result M′(T) is shown in Figure 33. The convolution has been performed to model the spatial resolution introduced by the PSF function of a given component. On analyzing the figures the convoluted signal M′(T) pertaining to PSF1 with f# = 4.0 induces a greater distortion into the input signal as compared to the optical system with f# = 2.3. This is validated by the calculations performed previously for the object space resolutions.

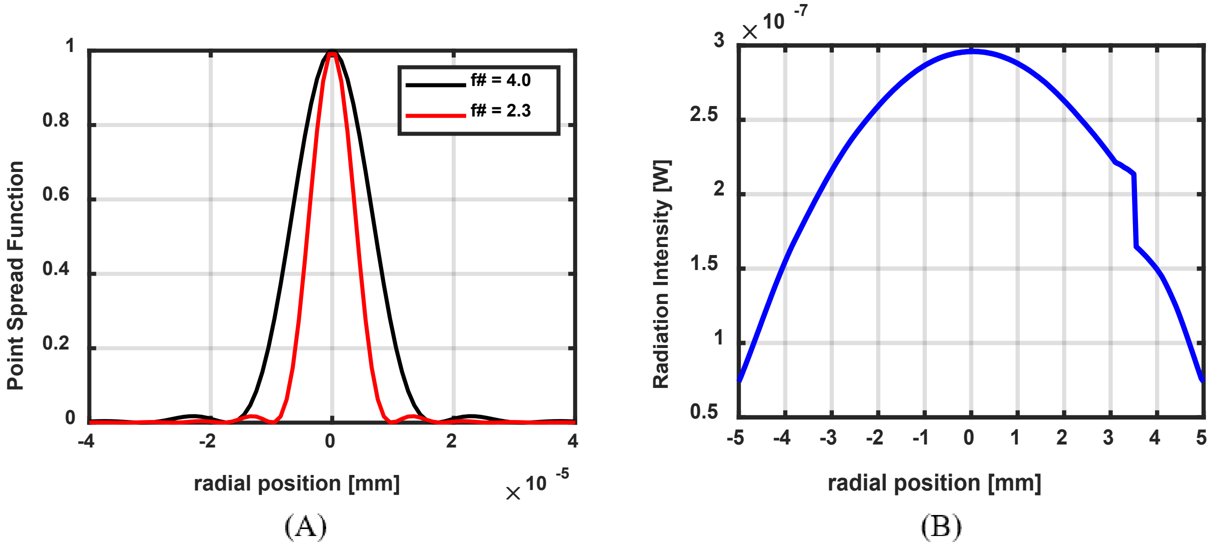

Figure 32: Distortion in optical system (A) PSF functions f# = 4.0, 2.3 (B) Intensity (M (T))

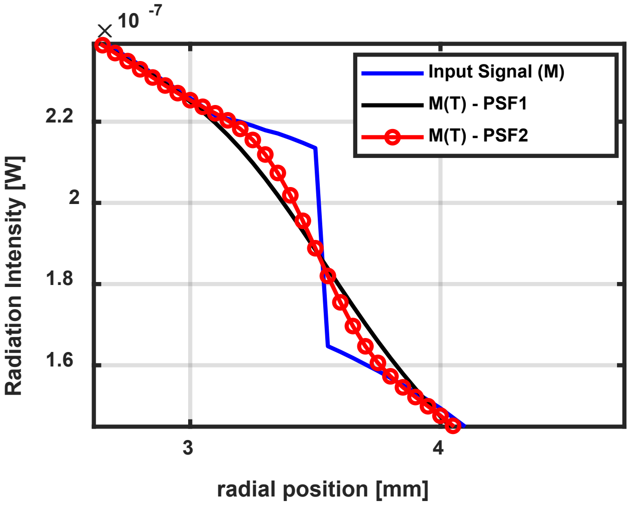

Figure 33: Input Signal and distorted signals M′(T), for, PSF1 (f# = 4.0), PSF2 (f# = 2.3)

3.1.4 Performance parameters – Thermal Sensitivity

The thermal sensitivity refers to the minimum temperature difference which can be resolved by the IR camera. The thermal sensitivity depends upon the light gathering properties of the camera, responsivity of the detector, noise of the system. The noise in the system is introduced due to various components such as the detectors, sensors, signal processing system, electronic circuit etc [48]. The sensor has inherent noise due to the level of illumination and its own temperature, and the electronic circuits connected to the sensor inject their own share of electronic circuit noise. The quantitative measurement of the thermal sensitivity is given by the Noise Equivalent temperature difference (NETD). A smaller value of NETD indicates a better thermal sensitivity. For example, an IR camera with NETD of 20mK has a better thermal sensitivity than an IR camera with NETD of 50mK, as it can resolve a temperature difference (ΔT) of 20mK as compared to ΔT of 50mK in the infrared thermal image.

$$\mathrm{NETD} = \left(4\mathrm{F}^2\sqrt{\Delta \mathrm{f}}/\sqrt{\mathrm{A_D}}\left[\frac{\Delta \mathrm{M}}{\Delta \mathrm{T}}\right]\tau_{\mathrm{optics}}\,\mathrm{D}^*\right) \tag{12}$$

Here Δf is the electronic bandwidth and D* is the normalized detectivity. The normalized detectivity is another important parameter used to specify the detector performance.

$$\mathrm{D}^* = \left(\frac{\sqrt{\mathrm{A_d}\,\Delta \mathrm{f}}}{\mathrm{NEP}}\right)\frac{\mathrm{cm}\,\sqrt{\mathrm{Hz}}}{\mathrm{Watts}} \tag{13}$$

The normalized detectivity is inversely related to the Noise Equivalent Power (NEP) of the detector. The NEP is the minimum radiant flux necessary to give an output signal equal to the detector noise. Now consider an IR camera having NEP value of 3.46×10^{-13} W. This NEP value indicates the noise generated by the IR camera due to various components like detectors, sensors, signal processing system, electronic circuit etc. For a meaningful output signal, the camera output should be greater than the NEP value of 3.46×10^{-13} W, else the signal will be distorted by the noise generated by the IR camera.

Now consider two imaging systems operating in the SWIR region (0.9 – 1.7 μm). The NETD, NEP values are 20mK, 3.46×10^{-13} W and 80mK, 7.23×10^{-13} W respectively. Consider a uniform surface heating of: - $\mathrm{P} = [1 + 0.05 \times \sin(\pi\, \mathrm{f_o t})]\ \mathrm{mW}$ with f = 0.01 Hz, on a crack geometry (Figure 13(B), Section 2.2). The first set of modelling results are found considering a background temperature ($\mathrm{T_b}$) of 300 K. The temperature profile and the radiation intensity input to the IR camera is shown in Figure 34. The corresponding output radiation signals from the two imaging systems is shown in Figure 35. Analyzing the figure 35, the signal is completely distorted, as the radiation intensity has a maximum of 1.29×10^-14 W which is less than the NEP values of both the IR system 1 and IR system 2.

The next set of modelling results are found considering a $\mathrm{T_b}$= 600 K. The temperature plot and the radiation intensity input to the IR camera are shown in Figure 36(A) and (B) respectively. The corresponding output radiation signals from the two imaging systems is shown in Figure 37. Analyzing Figure 37, the crack is detected in the IR system 1 configuration (20 mK, 3.46×10^{-13} W). However the crack is still not clearly detected in the IR system 2 configuration(80 mK, 7.23×10^{-13} W). Here even though the radiation magnitude is greater than the NEP values, the NETD value is so high that the small temperature differences cannot be efficiently resolved by the imaging system and hence the signal appears to be as distorted.

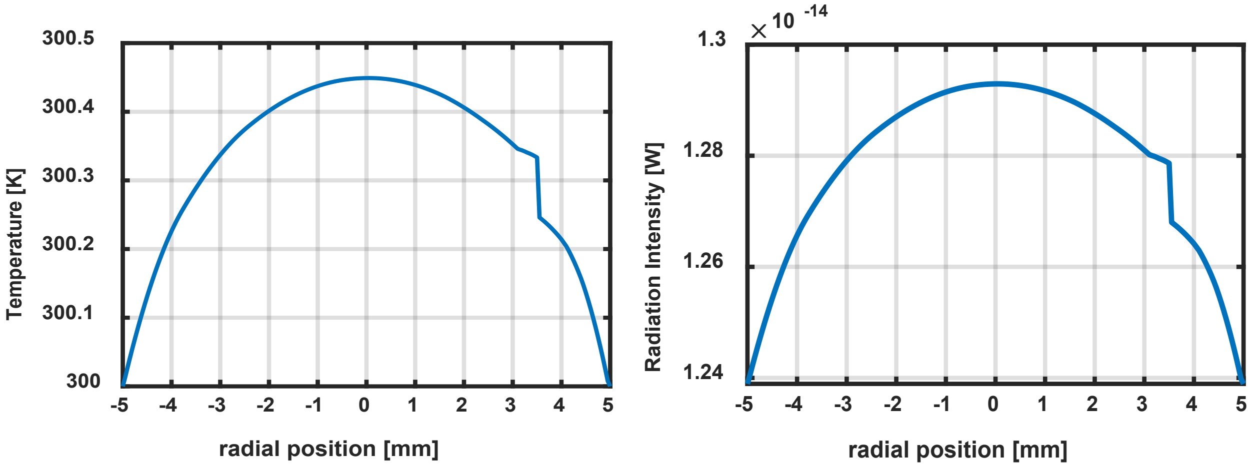

(A) (B)

Figure 34: Radiation Intensity modelling for T_b = 300 K, SWIR camera (0.9 – 1.7 μm) (A) Temperature line plot (B) Input Radiation Intensity to the IR Camera,

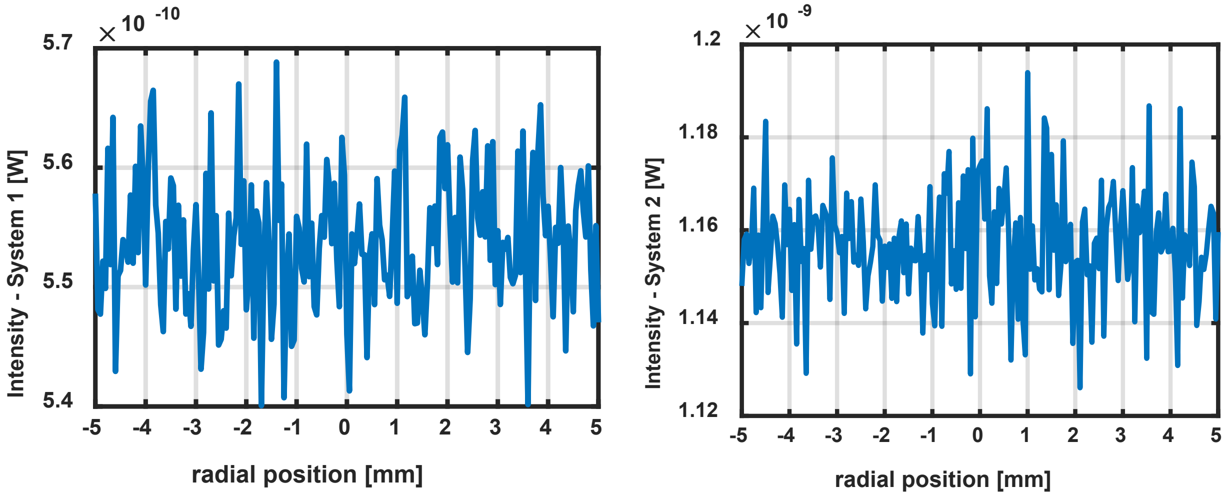

(A) (B)

Figure 35: Comparison of radiation intensity plots for T_b = 300 K, SWIR (0.9 – 1.7 μm) (A) Radiation plot for IR System 1, NETD = 20mK, NEP = 3.46×10^{-13} W, (B) Radiation plot for IR Imaging System 2, NETD = 80mK, NEP = 7.23×10^{-13} W,

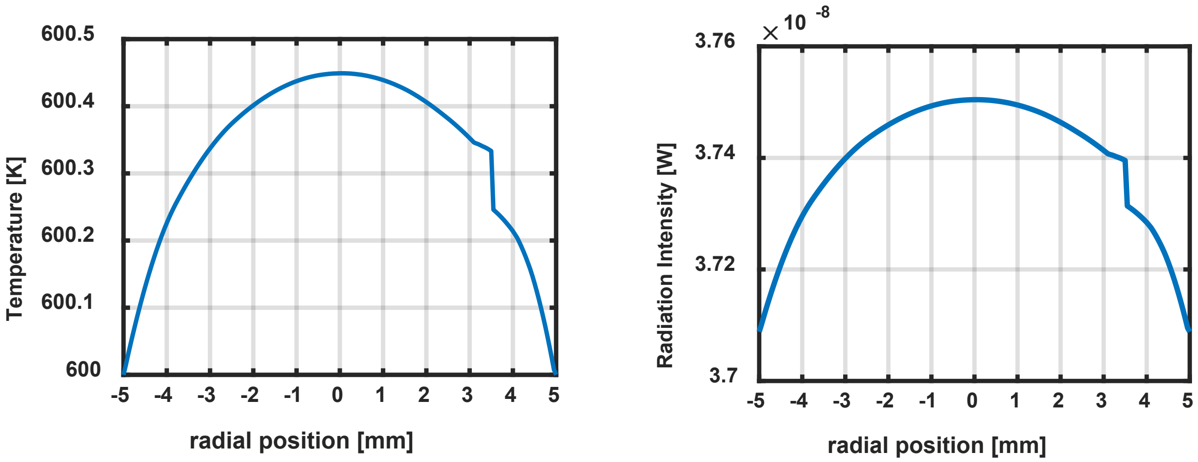

(A) (B)

Figure 36: Radiation Intensity modelling for T_b=600 K, SWIR camera (0.9 – 1.7 μm) ((A) Temperature line plot (B) Input Radiation Intensity to the IR Camera

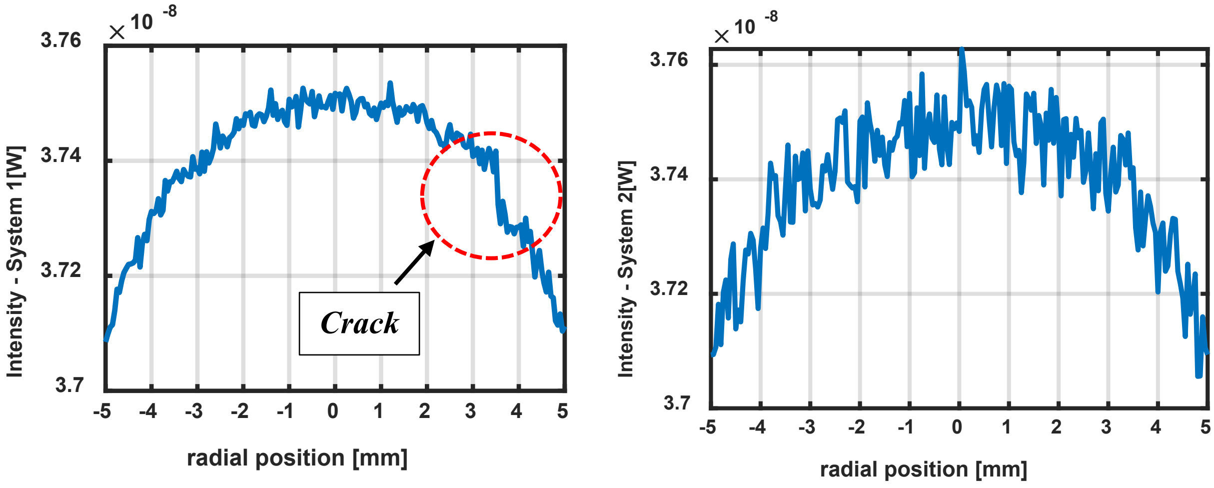

(A) (B)

Figure 37: Comparison of radiation intensity plots for $T_b = 600$ K, SWIR (0.9 – 1.7 μm) (A) Radiation plot for IR System 1, NETD = 20mK, NEP = 3.46×10^{-13} W, (B) Radiation plot for IR Imaging System 2, NETD = 80mK, NEP = 7.23×10^{-13} W

3.1.5 Signal to Noise Ratio (SNR)

The Signal to Noise Ratio (SNR) is a quantitative measure to define the crack visibility in the radiation intensity profiles. The SNR is defined as: -

$$\mathrm{SNR} = \Delta \mathrm{I}_{\mathrm{signal}}/\mathrm{I}_{\mathrm{noise}} \tag{14}$$

Here $\Delta \mathrm{I}_{\mathrm{signal}}$ is defined as the drop in signal magnitude across the crack and $\mathrm{I}_{\mathrm{noise}}$ is defined as the magnitude of noise in the vicinity of the crack. For crack visibility the magnitude of $\Delta \mathrm{I}_{\mathrm{signal}}$ should be greater than the magnitude of $\mathrm{I}_{\mathrm{noise}}$. Hence for SNR > 1, the crack is quantifiable and for SNR < 1 the crack is not quantifiable. Figure 38 plots the radiation intensity plots shown in Figure 37, however they are superimposed with the noise free (NETD = 0K, NEP = 0 W) radiation intensity plots for each of the cases.

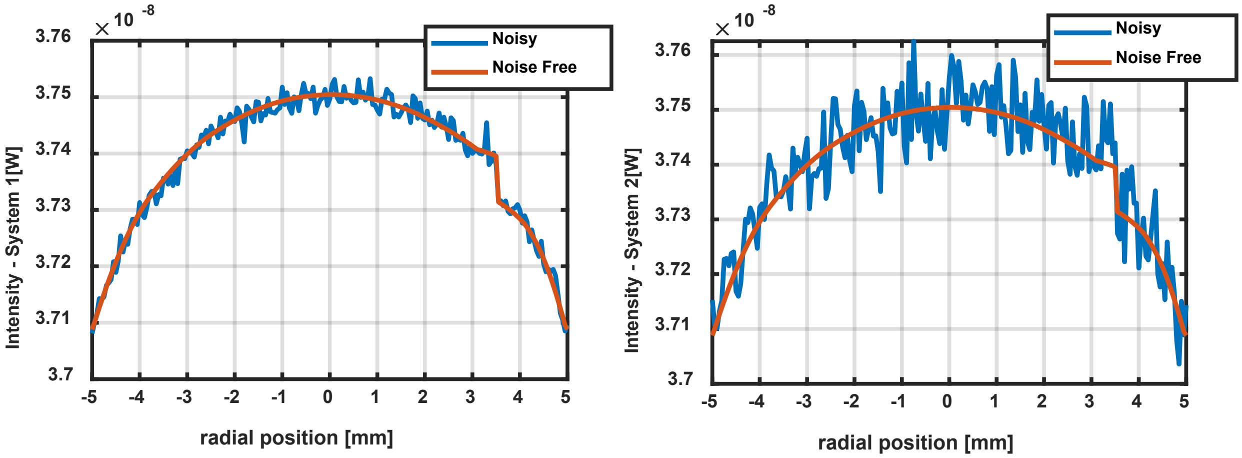

(A) (B)

Figure 38: Superimposed noisy/noise free radiation plot for $\mathrm{T_b} = 600$ K, SWIR (0.9 – 1.7 µm) (A) IR System 1 (20mK, 3.46×10^{-13} W), (B) IR System 2 (80mK, 7.23×10^{-13} W),

Visually analyzing the Figures 38 (A) and (B), the crack is quantifiable in Figure 38(A) and non-quantifiable in Figure 38(B). Quantitatively for Figure 38(A) the values of ΔI_{signal} and I_{noise} across the crack are 8.15×10^{-11}W and 5.27×10^{-11}W respectively, yielding a SNR value of 1.5472. Moreover for the Figure 38(B) the values of ΔI_{signal} and I_{noise} across the crack are 8.15×10^{-11}W and 9.27×10^{-11}W respectively, yielding a SNR value of 0.8798. The results from quantitative analysis indicate that the crack is quantifiable in Figure 38(A) and non-quantifiable in Figure 38(B). Hence the quantitative analysis seems to be in good agreement with the visual analysis and SNR can be used as a quantitative measure for defining the crack visibility.

3.1.6 Modelling of Thermal Sensitivity and Spatial Resolution

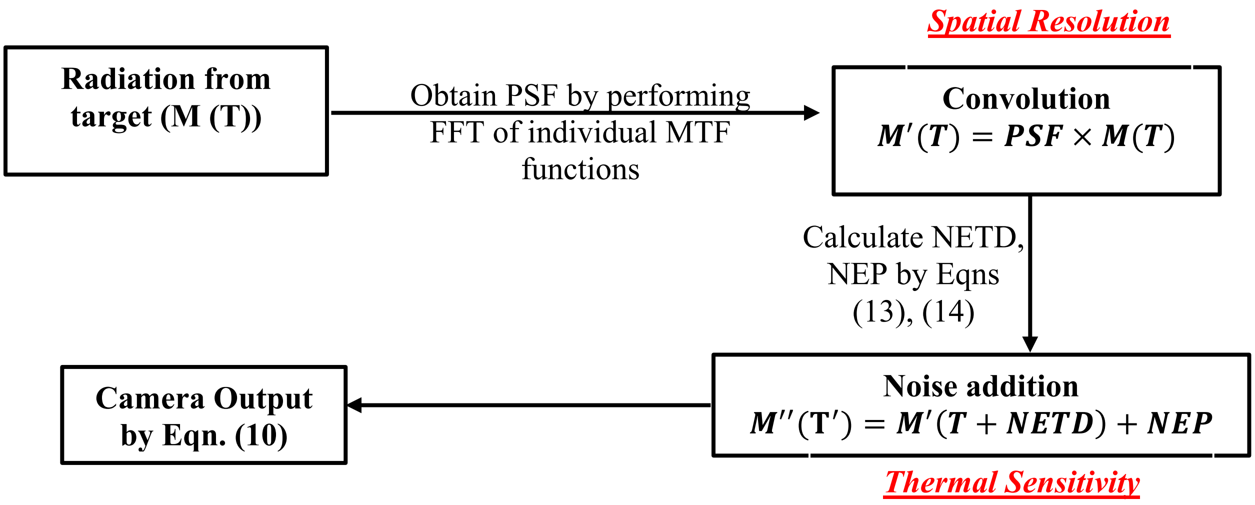

Figure 39: Modelling of Thermal Sensitivity and Spatial Resolution

The complete modelling process for the IR camera for the thermal sensitivity and spatial resolution is shown in Figure 39. As a first step the system PSF is calculated by performing FFT's of the individual MTF functions. Next the radiation from the target M(T) is convoluted with the PSF function to obtain $\mathrm{M}'(\mathrm{T})$. The NETD and the NEP are added next to quantify the thermal sensitivity of the camera. Finally the camera output is calculated on the basis of equation (10).

3.1.7 IR camera radiation modelling

The choice of the IR camera depends on a number of parameters namely: - Heating configuration (Figure 17, Section 2.2), Temperature range (Figure 21, 22 Section 2.3.2), Convolution due to the optical imaging system (Figure 32, 33, Section 3.1.2), NEP/NETD (Figure 34,35,36,37, Section 3.1.4). The choice of parameters is made on the basis of the configuration which maximizes the radiation signal and leads to the optimal value of the Signal to Noise Ratio (SNR) across the crack. Now considering the temperature profile shown in Figure 22(A) (Section 2.3.1) with $T_B = 600K$, the radiation intensity modelling is performed for different IR cameras as listed in Table 4. Modelling results performed previously (Figure 21, 22 Section 2.3.2) indicated that emissive power ($\mathrm{E_b}$) for the MWIR range > $\mathrm{E_b}$ for LWIR range > $\mathrm{E_b}$ for SWIR range. The modelling results for the radiation modelling are shown in Figures 40 and 41 for $\mathrm{T_b} = 600$ K. Here the SNR for the MWIR range (4.49) > SNR for SWIR range (1.42) > SNR for SWIR range (1.20).

Comparing the three cameras, the maximum value of SNR is obtained for the MWIR range as maximum value of E_b are observed and the IR camera induces moderate levels of noise and distortion (Table 4). Comparing the SNR values for the SWIR range and the LWIR range, higher SNR values are observed for the former. This can be attributed to the high noise/distortion levels introduced in the LWIR camera (Table 4), even though it has a higher E_b than the SWIR range.

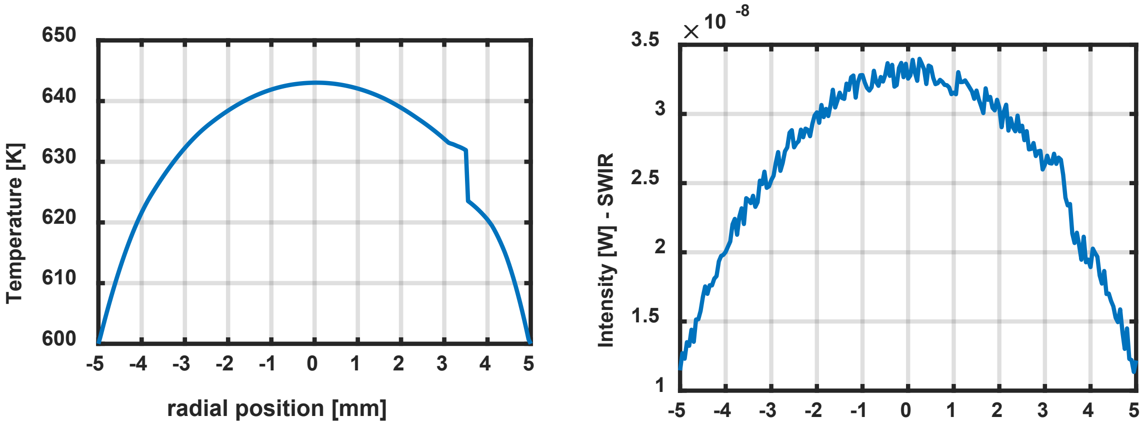

(A) (B)

Figure 40: Comparison of radiation intensity plots for $T_b = 600$ K (A) Temperature line plot, (B) Radiation Intensity for SWIR range (0.9 – 1.7 μm), (SNR = 1.42),

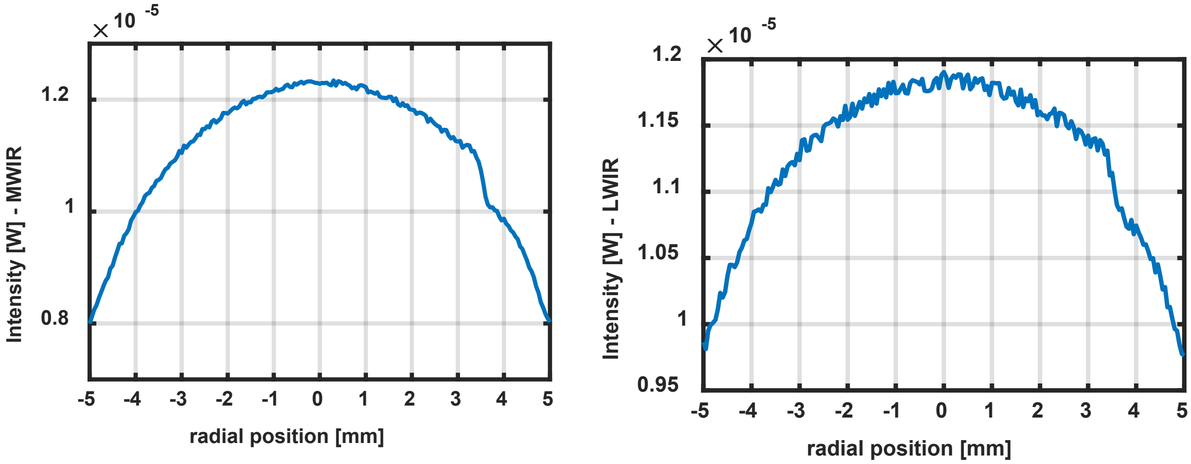

(A) (B)

Figure 41: Comparison of radiation intensity plots for $T_b = 600$ K (A) Radiation Intensity for MWIR range (2 – 5 μm) (SNR = 4.49), (B) Radiation Intensity for LWIR range (7 – 13 μm), (SNR = 1.20)

3.2 Lock in amplifier modelling

Lock in amplifier detection is a technique to extract the amplitude and the phase of a signal at a particular frequency from an output signal containing significant amount of noise levels at other frequencies. This helps in significantly boosting the signal to noise ratio and further enhancing the resolution of detection system. The block diagram for lock in amplifier is shown in Figure 42 [45].

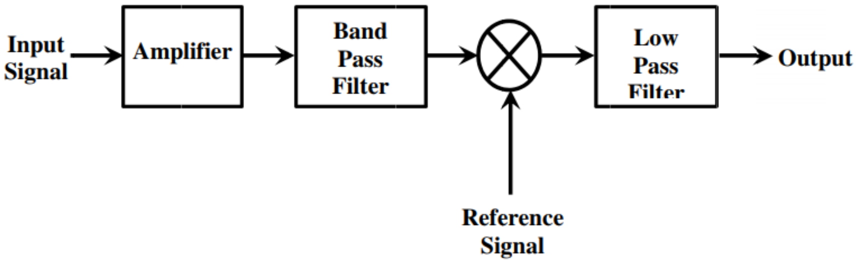

Figure 42: Block diagram of a lock in amplifier [45]

The lock in amplifier consists of an amplifier which is used to amplify the input signal following which it is fed through the band pass filter (BPF). The output of the BPF is multiplied with the reference signal (having desired measuring frequency) and then passed through the loss pass filter (LPF) to remove the unwanted frequency components present in the signal. The output signal is the amplitude and phase of the signal with the desired frequency.

3.2.1 Principle of Lock in Amplifier

The principle of the lock in amplifier can be understood on the basis of the equations presented below. Consider an input signal, 'V_{in}' and a reference signal 'REF': -

$$V_{in} = A_0 + A_1 \times \sin(\omega t + \emptyset_1) + A_2 \times \sin(2\omega t + \emptyset_2) \tag{15}$$

$$\mathrm{REF} = \sin(\omega t) \tag{16}$$

Here the input signal consists of a total of two components. The first component has a frequency, amplitude and phase of ω, A_1 and $\emptyset_1$ respectively. The second component has a frequency, amplitude and phase of 2ω, A_2 and $\emptyset_2$ respectively. Here using the lock in amplifier, the aim is to determine the amplitude and the phase of the signal at frequency ω in the input signal. The reference signal has been considered to have a frequency, ω. Now the input signal is multiplied and integrated with two versions of the reference signal to give intermediate signals, X and Y called as the inphase and the out of phase components respectively.

$$X = \frac{1}{T}\int_0^T V_{in} \times \sin(\omega t)\, dt \tag{17}$$

$$X = \frac{1}{T}\int_0^T [A_0 \sin(\omega t) + A_1 \sin(\omega t + \emptyset_1) \sin(\omega t) + A_2 \sin(2\omega t + \emptyset_2) \sin(\omega t)]\, dt \tag{18}$$

$$X = \frac{1}{T}\int_0^T \left[A_0 \sin(\omega t) + \frac{A_1}{2}[\cos(\emptyset_1) - \cos(2\omega t + \emptyset_1)] + \frac{A_2}{2}[\cos(\omega t + \emptyset_2) - \cos(3\omega t + \emptyset_2)]\right] dt \tag{19}$$

Here for equation (19) its important to note that all the cosine/sine terms with a frequency term, when integrated from a time period of 0 to T are equal to 0. $\int_0^T \sin(\omega t), \cos(2\omega t + \emptyset_1), \cos(\omega t + \emptyset_2), \cos(3\omega t + \emptyset_2)\, dt = 0$. Hence the equation (19) reduces to: -

$$X = \frac{A_1}{2}[\cos(\emptyset_1)] \tag{20}$$

Similarly now the calculation has been performed for the out of phase component Y_{90}: -

$$Y = \frac{1}{T}\int_0^T V_{in} \times \cos(\omega t)\, dt \tag{21}$$

$$Y = \frac{1}{T}\int_0^T [A_0 \cos(\omega t) + A_1 \sin(\omega t + \emptyset_1) \sin(\omega t) + A_2 \sin(2\omega t + \emptyset_2) \sin(\omega t)]\, dt \quad (22)$$

$$Y_0 = \frac{1}{T}\int_0^T \left[A_0 \cos(\omega t) + \frac{A_1}{2}[\sin(\emptyset_1) + \sin(2\omega t + \emptyset_1)] + \frac{A_2}{2}[\sin(\omega t + \emptyset_2) + \sin(3\omega t + \emptyset_2)]\right] dt \quad (23)$$

Here as shown previously, for equation (23) its important to note that all the sine/cosine terms with a frequency term, when integrated from a time period of 0 to T are equal to 0. Hence the equation (23) reduces to: -

$$Y = \frac{A_1}{2}[\sin(\emptyset_1)] \quad (24)$$

Note that the phase ($\emptyset$) and amplitude (A), of the desired signal with frequency ω is given as: -

$$A_1 = 2(X^2 + Y^2)^{\frac{1}{2}} \quad (25)$$

$$\emptyset_1 = \tan^{-1}(Y/X) \quad (26)$$

3.2.2 Radiation IR Modelling with Lock in Amplifier

In section 3.2, the modelling of the IR camera involved accounting for spatial resolution and thermal sensitivity which lead to limitation in resolution of the infrared image. Under certain cases with high NETD, NEP values, crack detection poses a great challenge to the IR imaging system. Under section 3.2.3, Figure 37(B), the crack is non-quantifiable for the given system parameter with the radiation intensity plot yielding a SNR of 0.87. Under the same circumstances but using a lock in amplifier, the radiation intensity plot is now found using the lock in modelling equations (17) – (26). It is important to note that the lock in amplifier system outputs the radiation intensity corresponding to the AC component (T_ω) and ignores the DC components in the signal. Figure 43

(A), (B) plots the radiation intensity plots for an imaging system with and without a lock in amplifier respectively. NETD, NEP, T_b values for both the imaging systems are 80mK, 7.23×10^{-13} W and 600 K respectively. The crack is visible in the Figure 43(A) but not visible in the Figure 43(B). Quantitatively for Figure 43(A), (B) the SNR values are 2.03 and 0.87 respectively. Here the lock in amplifier enhances the SNR of the IR image and hence enhances the image resolution to overcome the system limiting parameters (high NEP, NETD values).

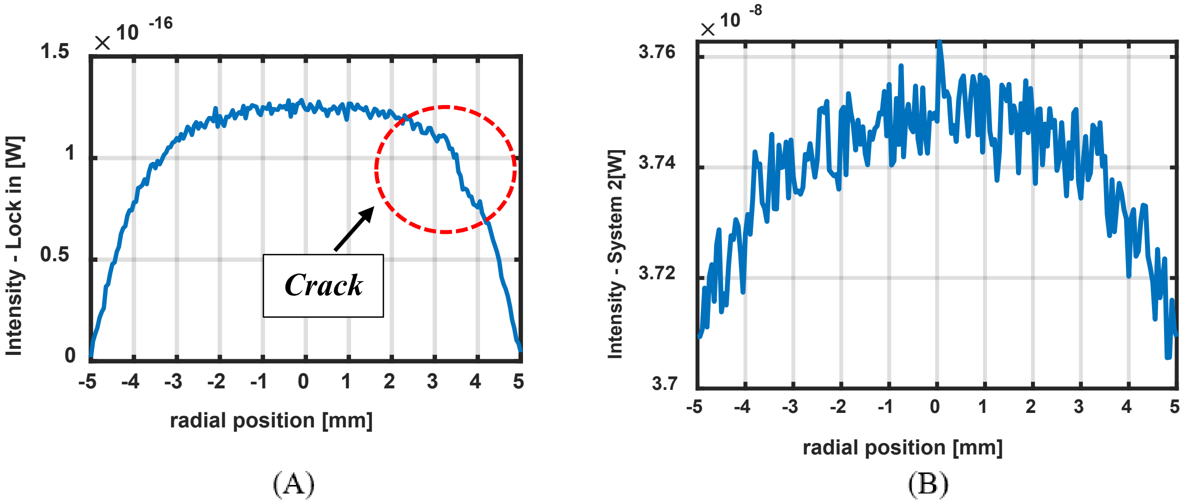

(A) (B)

Figure 43: Amplification of SNR by a lock in amplifier for $T_b = 600$ K, SWIR (0.9 – 1.7 µm), NETD = 80mK, NEP = 7.23×10^{-13} W (A) Radiation Intensity plot for system with lock in module (Lock in Signal), (SNR = 2.03) (B) Radiation Intensity plot for system without lock in module, (SNR = 0.87)

Chapter 4: IN-PILE, LABORATORY ENVIRONMENT CRACK MODELLING

4.1 In pile imaging

The modelling results presented here corresponds to thermal imaging for in-pile experiments inside the reactor environment under uniform heating using an InSb camera MWIR (2 – 5 µm). Uniform heating is achieved due to either neutron or gamma absorption. The camera parameters for the MWIR camera are specified in the Table 4 (Section 3.1.1). The heating configurations under consideration are Case A and Case B as described in Table 1 (Section 2.2)**.** The configuration in case A is targeted for imaging under steady state conditions, while the configuration in case B is targeted for imaging using lock in thermography. Imaging under both configurations is performed using optical IR fiber bundles which acts a medium to transport information outside of reactor core to the imaging system. Ideally the attenuation coefficient value (α) of IR fiber bundles is α = 0.4 dB/m (Thor Labs). However since the fiber bundles are placed inside the harsh nuclear reactor, we have to account for the impact of the high temperatures and the radiation effects (gamnma rays and neutrons) [42]. For modelling purposes we assume a more conservative estimate of α = 1.2 dB/m. The length of fiber bundle is considered as 5 m. Using the attenuation equation for optical fiber bundles (10), for the given values of α and length the output signal from the optical fiber bundles undergoes a transmission loss of 74.88 %. For the modelling purpose, we have considered a cylinder shaped uranium dioxide ($\mathrm{UO_2}$) pellet material. The material properties of $\mathrm{UO_2}$ [32] and model/crack dimensions are listed in Table 2 (Section 2.2)**.**

The rate of energy release (power) due to the fission reaction is estimated based on the equation (27) shown below. Here P ($MeV.s^{-1}$) is the reactor power, Φ is the neutron flux ($neutrons. cm^2. s^{-1}$), N ($atoms. cm^{-3}$) is the atomic number density. σ (cm^2) is the microscopic cross section, E_r ($MeV. fission^{-1}$) is the average recoverable energy per fission and V (m^3) is the total volume of the core.

$$P = \Phi\ N_{U235}\ \sigma_f^{235}\ .E_r\ .V \tag{27}$$

The reactor power here is estimated based on a neutron flux of $10^{13} neutrons. cm^2. s^{-1}$ and with the UO_2 being made of natural uranium material. Performing the required calculation a uniform volumetric internal heating of 2 $\frac{\mathrm{W}}{\mathrm{cm}^3}$ is considered for the thermal model. Further a convection heat transfer coefficient of h = 10 $\frac{\mathrm{W}}{\mathrm{m}^2\mathrm{K}}$ is considered, by assuming Helium flow around the nuclear fuel pellet. For the lock in configuration, in addition to the uniform volumetric heat source ($\dot{\mathrm{Q}}$), a frequency modulated surface heating is considered, $\mathrm{q}'' = 5 \times \sin(\pi\ \mathrm{f_o t})$ nW/m^2, (f = 0.1), which is delivered to the fuel rod using the optical IR fiber bundle.

4.1.1 Results for Case (A) - Uniform heating within the solid with fiber bundle (Steady State)

The temperature contour profile for heating configuration (A) and the line plot for the probe line is shown in Figure 44. Note that a background temperature of 675 K is considered. The profile attains a maximum temperature value of 684.88 K. The crack is highlighted in red and shown in the temperature line plot. The corresponding radiation intensity profiles is shown in Figure 45 for the heating configuration (A) for $\mathrm{T_b}$ = 675K using a MWIR camera with parameters summarized in Table (4). The signal has noise/distortion and shows signs of crack visibility.

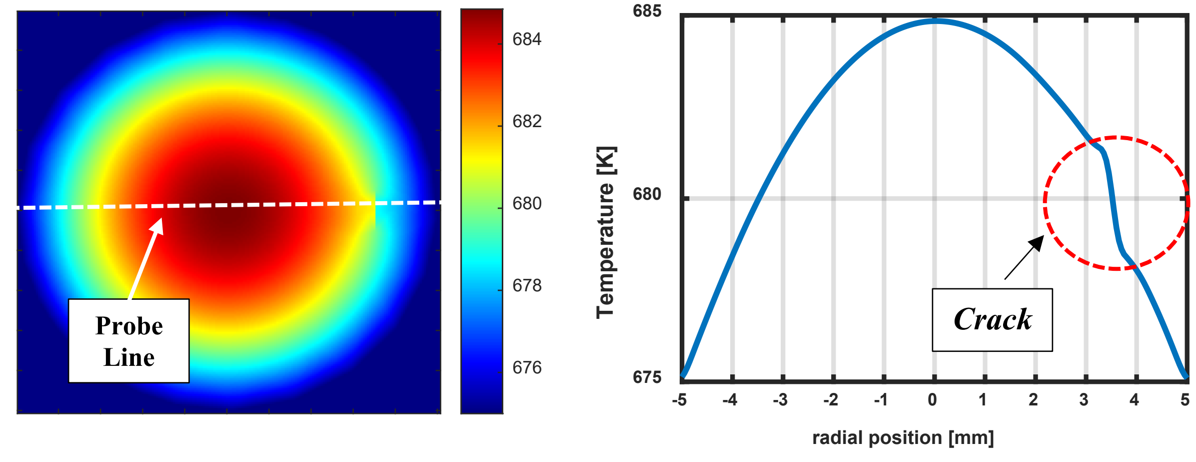

(A)

(B)

Figure 44: Radiation modelling results for heating configuration (A) for MWIR camera (2 – 5 μm) (A) Temperature contour plot, (B) Temperature line plot for probe line

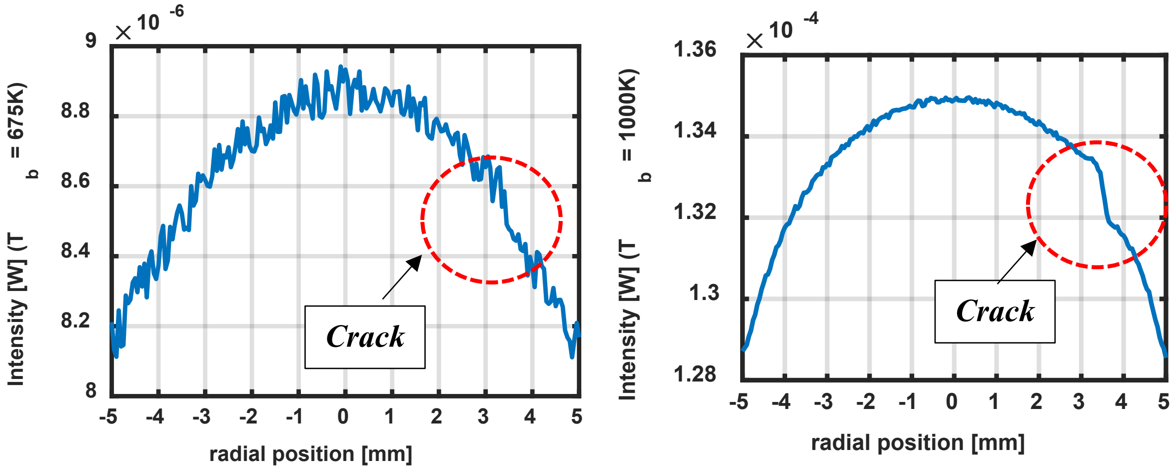

(A)

(B)

Figure 45: Radiation modelling results for heating configuration (A) for MWIR camera (2 – 5 μm) (A) T_b = 675 K (SNR = 1.01) (B) T_b = 1000 K (SNR = 3.26)

The SNR value for $T_b = 675$ K for heating configuration (A) for the radiation intensity profile in Figure 45(A) is 1.0186. The next set of results are plotted considering an elevated background temperature of 1000 K. The corresponding radiation intensity profiles is shown in Figure 45(B). Here the crack is clearly quantifiable as the radiation intensity signal has been amplified due to a higher temperature. The SNR value for $T_b = 1000$ K for heating configuration (A) for the radiation intensity profile in Figure 45(B) is 3.2667. Table 5 summarizes SNR values for $T_b =$ 300 K – 900 K. The radiation signal starts showing first signs of crack visibility around $T_b =$ 675K.

Table 5: Summary of SNR for heating configuration (A) for T_b= 300 K – 1000 K

T_b	300K	350K	400K	500K	550K	600K	650K	675K	700K	800K	1000K
SNR	0.047	0.014	0.044	0.23	0.36	0.41	0.72	1.01	1.55	2.71	3.26

4.1.2 Results for Case (B) - Uniform heating within the solid with fiber bundle (Lock in)

The temperature contour profile for heating configuration (B) and the line plot for the probe line is shown in Figure 46. Note that a background temperature of 675 K is considered. The profile attains a maximum temperature value of 686.04 K. The crack is highlighted in red and shown in the temperature line plot. The corresponding radiation intensity profiles is shown in Figure 47(A) using a MWIR camera with parameters summarized in Table (4). The crack is visible in the radiation profile with the SNR value of 2.49 for $T_b = 675$ K for heating configuration (B).

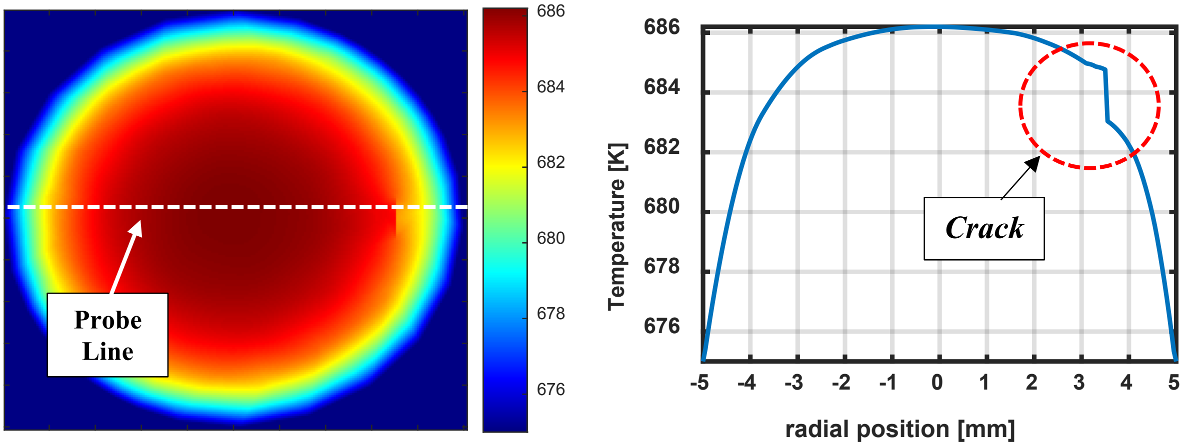

(A) (B)

Figure 46: Radiation modelling results for heating configuration (B) for MWIR camera (2 – 5 µm) (A) Temperature contour plot, (B) Temperature line plot for probe line

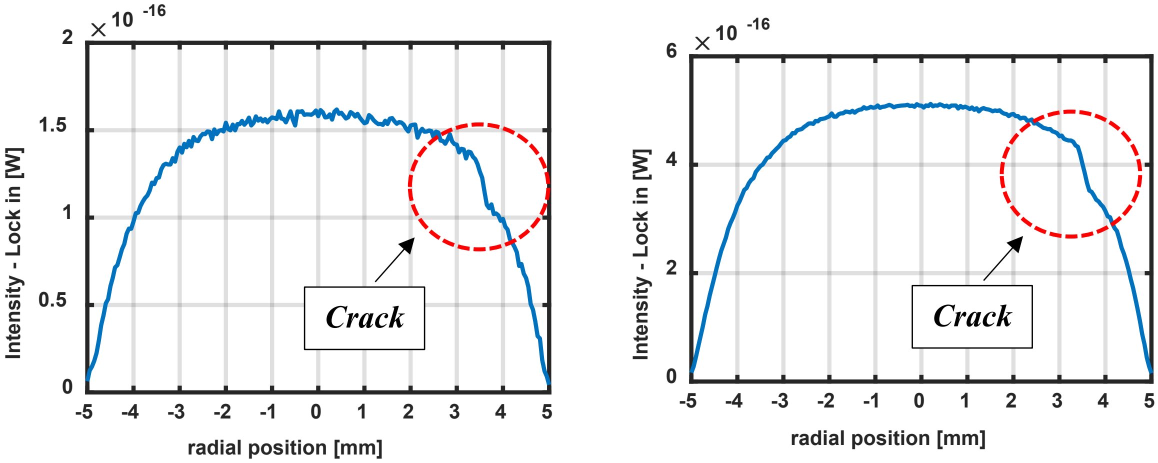

(A) (B)

Figure 47: Radiation modelling results for heating configuration (B) for MWIR camera (2 – 5 µm) (A) T_b = 675 K (SNR = 2.49) (B) T_b = 1000 K (SNR = 15.74)

Comparing SNR values between heating configuration (A) and (B) for T_b = 675 K, the heat configuration (B) has a much greater value. This can be attributed to the fact that heating configuration (B) includes a lock in amplifier.

The next set of results are plotted considering an elevated background temperature of 1000 K. The corresponding radiation intensity profiles is shown in Figure 47(B). Here the crack is clearly quantifiable and has a high SNR value of is 15.74. Comparing SNR values between heating configuration (A) and (B) for T_b = 1000K, the heat configuration (B) has a much greater SNR value. Table 6 summarizes SNR values for $T_b = 300$ K – 1000 K. The signal starts showing first signs of crack visibility around $T_b = 575$K.

Table 6: Summary of SNR for heating configuration (B) for T_b= 300 K – 1000 K

T_b	300 K	350 K	450 K	470 K	500 K	575 K	600 K	800 K	1000 K
SNR	0.023	0.089	0.41	0.59	0.67	1.01	1.68	6.72	15.74

4.2 Laboratory environment IR modelling

The modelling results presented here correspond to thermal imaging for crack detection in the laboratory environment with surface heating using an InSb camera MWIR (2 – 5 µm). The camera parameters for the MWIR camera are specified in the Table 4 (Section 3.1.1). The heating configurations under consideration are Case C and Case D as described in Table 1 (Section 2.2). The heating configuration C and D are targeted for thermal imaging under steady state conditions and using lock in thermography respectively. For the modelling purpose, we have considered a cylinder with uranium dioxide (UO_2) material. The material properties of UO_2 [32] and model/crack dimensions are listed in Table 2 (Section 2.2).

For the steady state configuration (Case (C)), a uniform surface heating of 100 mW is considered on the top surface along with convection boundary conditions on the adjacent outer surfaces. Since conditions inside a laboratory environment are to be simulated, a free convection coefficient of h = 10 $\frac{W}{m^2K}$ is considered. For the lock in configuration, a frequency modulated surface heating of $q'' = 50 \times \sin(\pi\, f_o t)$ mW/m^2, (f = 0.2 Hz) is considered in addition to the uniform surface heating of 100 mW. A free convection heat transfer coefficient of h = 10 $\frac{W}{m^2K}$ is considered on the outer adjacent surfaces in heating configurations (D).

4.2.1 Results for Case (C) - Uniform surface heating (Steady State)

The preliminary results for case (C) are presented for the uniform surface heat steady state conditions for a background temperature of 500 K. The temperature line profile and the intensity profile is shown in the Figure 48. The temperature profile attains a maximum value of 510.8 K which the crack highlighted in red. Observing the corresponding intensity profile for the steady state case for T_b = 500 K using a MWIR camera (Table (4)), the signal has noise/distortion and shows signs of crack visibility. The SNR value for $T_b = 500$ K for heating configuration (C) for the radiation intensity profile in Figure 49(A) is1.11.

The next set of results are plotted considering an elevated background temperature of 1000 K. The corresponding radiation intensity profiles is shown in Figure 49(B). Here the crack is clearly quantifiable as the radiation intensity signal has been amplified due to a higher temperature.

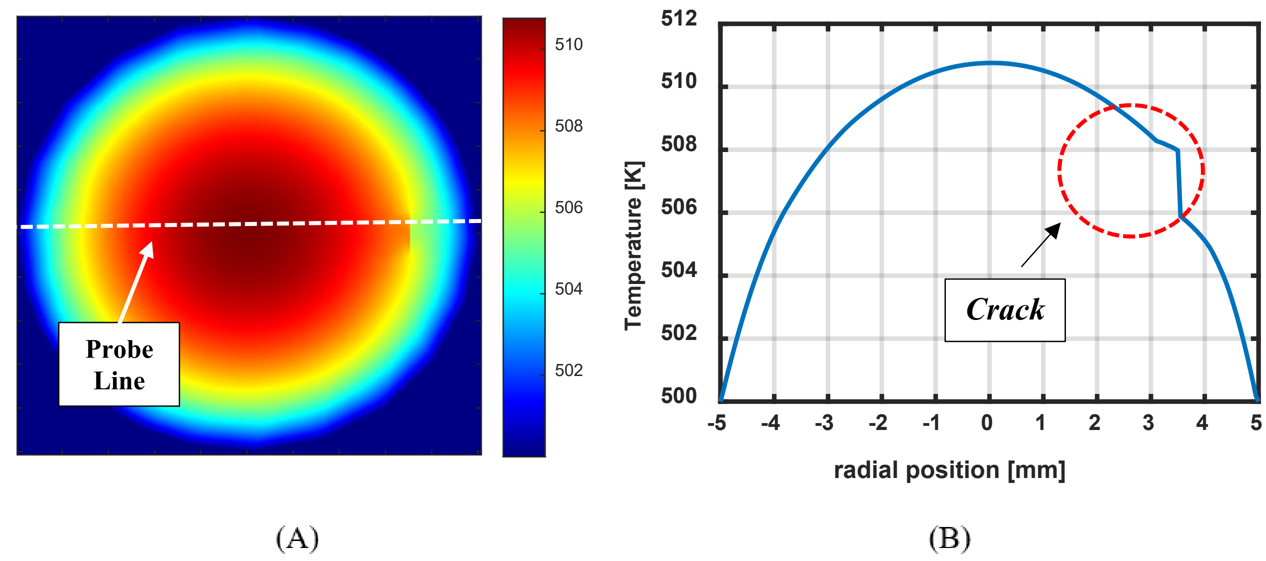

Figure 48: Radiation modelling results for heating configuration (C) for MWIR camera (2 – 5 µm) (A) Temperature contour plot $T_b = 500\ K$, (B) Temperature line plot for probe line

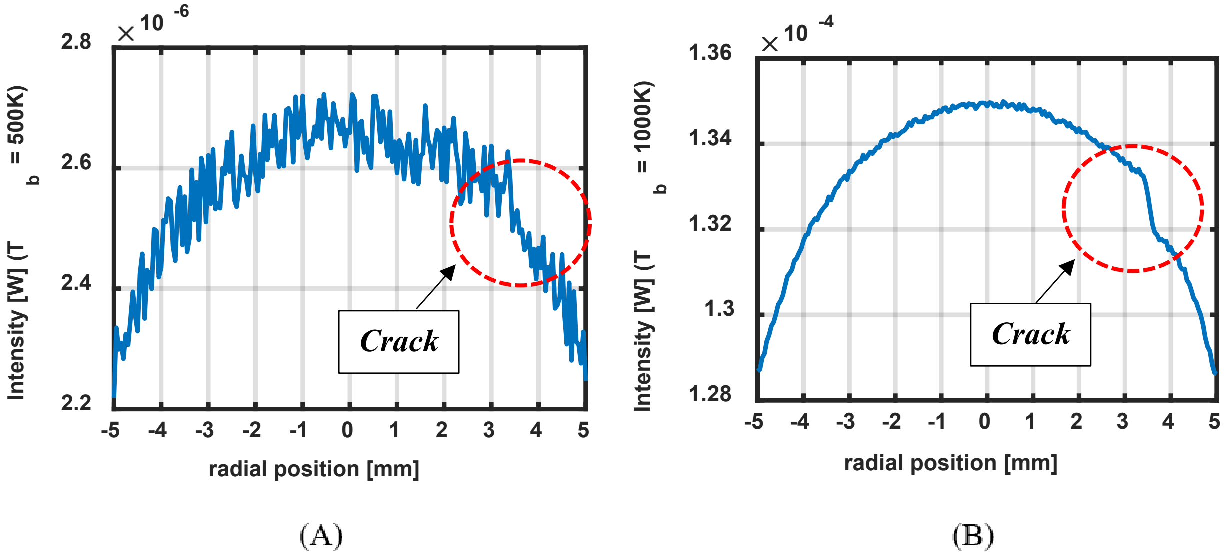

Figure 49: Radiation modelling results for heating configuration (C) for MWIR camera (2 – 5 µm) (A) $T_b = 500$ K (SNR = 1.11) (B) $T_b = 1000$ K (SNR = 6.72)

The SNR value for $T_b = 1000$ K for heating configuration (C) for the radiation intensity profile in Figure 45(B) is 6.72. Table 7 summarizes SNR values for $T_b = 300$ K – 1000 K. The radiation signal starts showing first signs of crack visibility around $T_b = 490$ K.

Comparing the results for heating configuration (A) and (C) involving steady state configurations, for a given value of T_b the SNR for heating configuration (C) has a greater value. This is because heating configuration (A) operates under reactor environment conditions and utilizes optical fiber bundles to assist in thermal imaging. Hence this leads to high transmission losses in the range of 60 – 80 %.

Table 7: Summary of SNR for heating configuration (C) for T_b= 300 K – 1000 K

T_b	300K	350K	400K	470K	490K	500K	550K	600K	700K	800K	1000K
SNR	0.031	0.11	0.31	0.89	1.01	1.10	1.46	2.16	3.07	3.82	6.72

4.2.2 Results for Case (D) - Uniform surface heating (Steady State)

The initial results for case (D) are presented for the uniform surface heat steady state conditions for a background temperature of 500 K. The temperature line profile and the intensity profile is shown in the Figure 48. The temperature profile attains a maximum value of 511.1 K which the crack highlighted in red. Observing the corresponding intensity profile Figure 51(A), for the steady state case for T_b = 500 K using a MWIR camera (Table (4)), the signal has a SNR value of 1.71 with the crack being quantifiable with traces of noise/distortion. Comparing SNR values between heating configuration (C) and (D) for T_b = 500 K, the heat configuration (D) yields a greater value due to the lock in amplifier.

The next set of results are plotted considering an elevated background temperature of 1000 K. The corresponding radiation intensity profiles is shown in Figure 51(B). Here the crack is clearly quantifiable as the radiation intensity signal has been amplified due to a higher temperature. The SNR value for $T_b = 1000$ K for heating configuration (D) for the radiation intensity profile in Figure 51(B) is 18.5. Table 8 summarizes SNR values for $T_b = 300$ K – 1000 K. The radiation signal starts showing first signs of crack visibility around $T_b = 430$ K.

Table 8: Summary of SNR for heating configuration (D) for T_b= 300 K – 1000 K

T_b	300K	350K	400K	425K	435K	475K	550K	600K	700K	800K	1000K
SNR	0.034	0.19	0.44	0.77	1.13	1.56	1.71	3.75	6.45	9.76	18.49

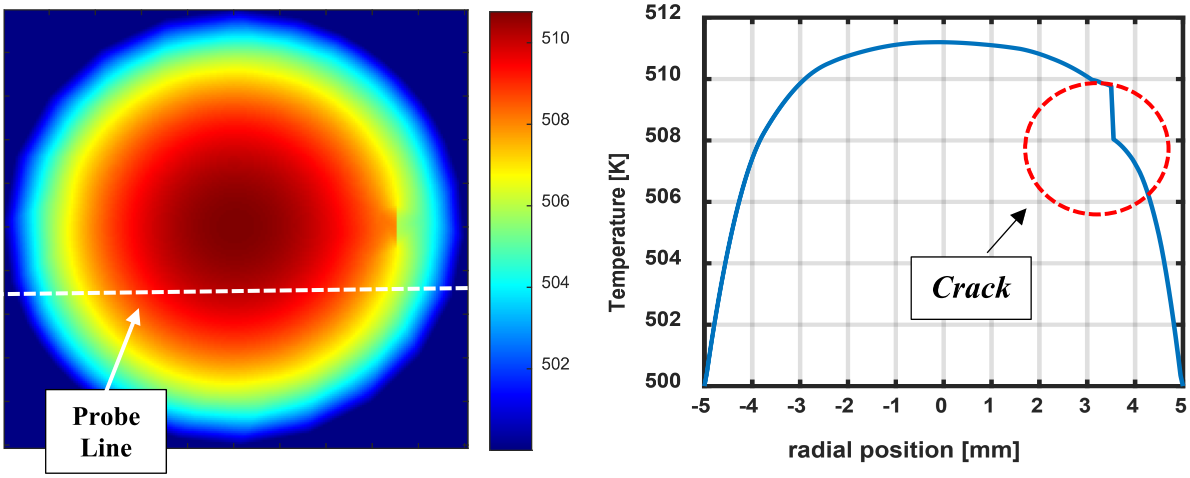

(A) (B)

Figure 50: Radiation modelling results for heating configuration (D) for MWIR camera (2 – 5 µm) (A) Temperature contour plot $T_b = 500\ K$, (B) Temperature line plot for probe line

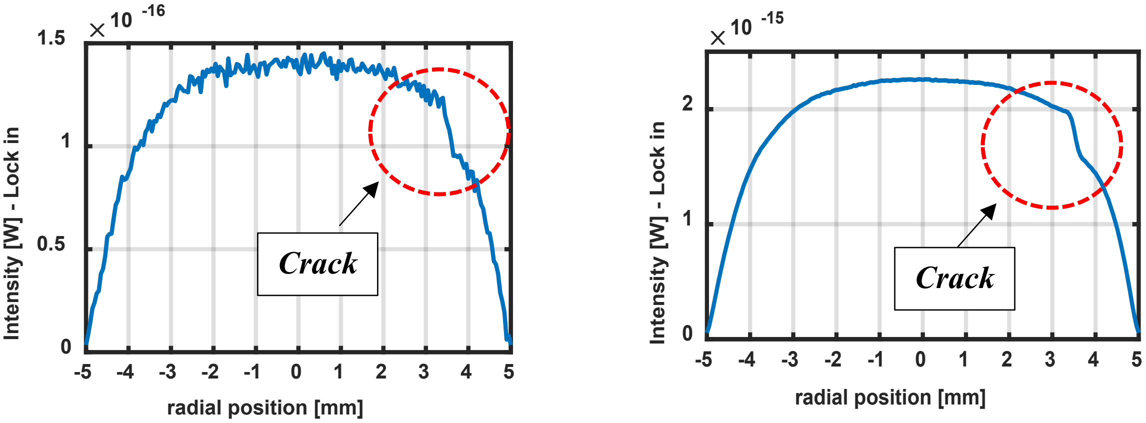

(A) (B)

Figure 51: Radiation modelling results for heating configuration (C) for MWIR camera (2 – 5 µm) (A) T_b = 500 K (SNR = 1.71) (B) T_b = 1000 K (SNR = 18.5)

4.3 Summary of in-pile and laboratory environment IR modelling

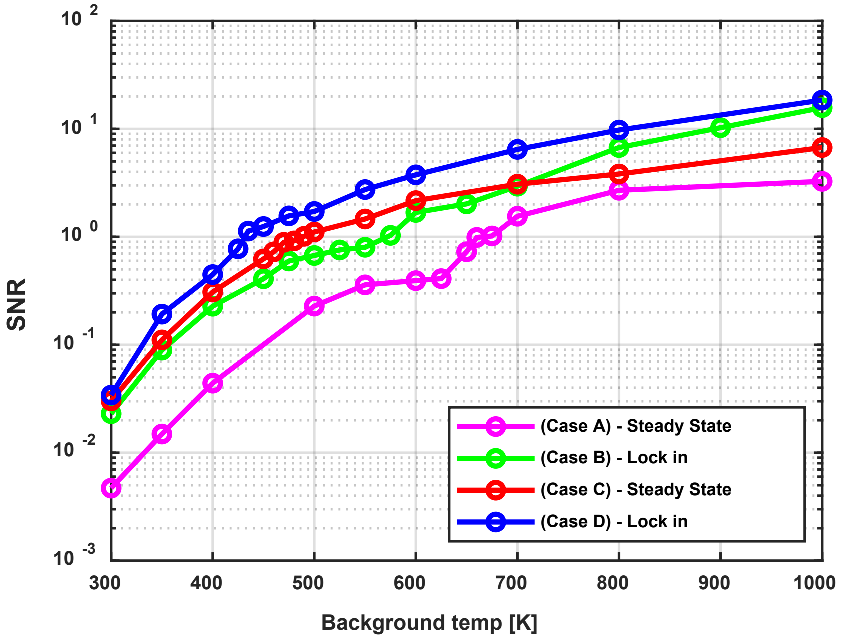

Figure 52: SNR vs Tb plot for Case A, B, C and D for Tb range from 350 K to 1500 K

Table 9: Summary of SNR ratio for in-pile/laboratory environment conditions, Case (A), (B), (C), (D)

T_b	**300K**	**400 K**	**500 K**	**600 K**	**700 K**	**800 K**	**1000 K**
SNR (Case A)	0.0047	0.044	0.22	0.39	1.55	2.71	3.75
SNR (Case B)	0.023	0.22	0.67	1.68	2.94	6.72	15.74
SNR (Case C)	0.031	0.31	1.71	2.16	3.01	3.82	6.72
SNR (Case D)	0.034	0.44	1.10	3.75	6.45	9.76	18.49

A summary of the SNR ratios for the cases (A), (B), (C) and (D) is presented in Table 9. Additionally a line plot superimposing all the 4 cases is shown in Figure 52, for different values of background temperature. On the basis of the results obtained in Figure 52, a study was conducted to identify the SNR cutoff value for which the crack is identifiable in the radiation intensity line plots. It is important to note that these results hold true for the given camera parameters and configurations i.e. InSb IR Camera (2 – 5 µm), NETD = 50 mK, NEP = 70 nW. The following observations were made: -

- For each of the heating configurations, the cracks starts to show signs of visibility for a T_b corresponding to SNR > 1. For heating configurations, (A), (B), (C), (D), the T_b for which SNR ≈ 1 is 675 K, 575 K, 490 K and 430 K respectively.
- The slope for the lock in heating configurations (B), (D) is greater than the slope for the steady state configurations. For the steady state configurations, the SNR values increase linearly w.r.t the background temperature. However for lock in configurations, the SNR values display an exponential rise. For example at $T_b = 300$ K, the SNR values for heating configuration (A) (Steady State) and heating configuration (B) (Lock in) are 0.0047 and 0.023 respectively. However when the T_b is raised to 1000 K, the SNR values for heating configuration (A) (Steady State) and heating configuration (B) (Lock in) are 3.75 and 15.74 respectively. The lock in configurations displays a much greater increase in SNR as compared to the steady state configuration.

As mentioned previously, the SNR results in Table 9 and Figure 52 are true for the given camera configuration and parameters (InSb IR Camera (2 – 5 µm), NETD = 50 mK, NEP = 70 nW). To highlight the sensitivity of the signal to the camera parameters, a comparison study has been performed between two InSb cameras (2 – 5 µm) with different values of NEP and NETD. The two parameters for the two cameras is summarized in the Table 10. The SNR vs Tb plot for the two IR cameras is shown in the Figure 53 for a temperature range of 300 to 1000 K for Case C, D. As observed in Figure 53, the best results are obtained for Case D, (IR Camera 2). The SNR values for Case D (IR Camera 2) are comparable to the SNR values for Case C (IR Camera 1). Lastly worst results are obtained for the Case C (IR Camera 1).

Table 10: Important parameters for IR Camera Configuration 1 and 2

IR Camera 1	InSb, MWIR, (2 – 5 µm)	NETD = 500 mK	NEP = 200 nW
IR Camera 2	InSb, MWIR, (2 – 5 µm)	NETD = 50 mK	NEP = 70 mW

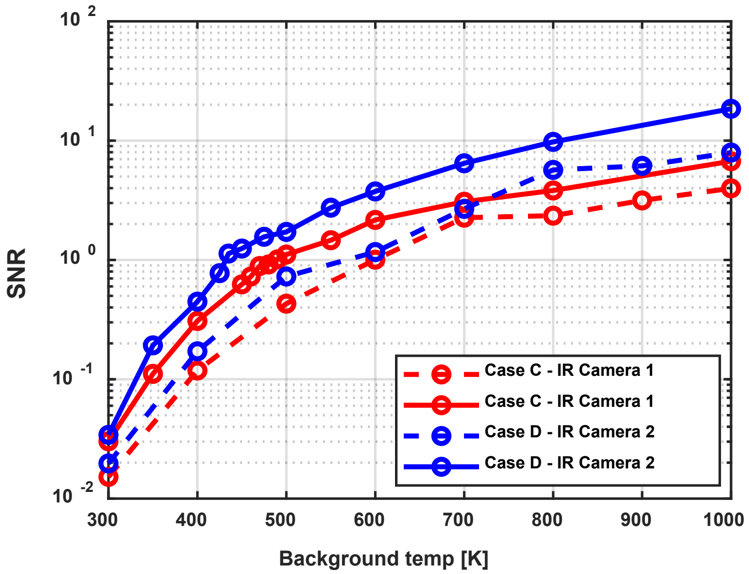

Figure 53: SNR vs Tb plot for Heating Configuration C, D for IR Camera Configurations 1,2 with parameters summarized in Table 10

Chapter 5: REALISTIC CRACK MODELLING

5.1 Model Description

An IR thermography model has been developed to simulate IR modelling for realistic cracks. For modelling purpose, we have considered a cylinder with CeO_2 material. The material properties of CeO_2 [49] and the model dimensions are summarized in Table 11. The cracked model with the radial and longitudinal cracks is shown in Figure 54.

The heating configuration (C) (Uniform surface heating (Steady State) here under laboratory conditions) as mentioned in Table 1 (Section 2.1) is chosen as the configuration for crack detection. The only exception being that a point surface gaussian heating is considered here instead of a uniform surface heating. Hence for the given configuration, the relevant thermal governing equation and the boundary conditions are presented in Table 12.

Note that a point surface gaussian heating of $P = 5$ W, is considered on the top surface of the crack model. Additionally convective boundary conditions have been considered on the outer adjoining surfaces. Since conditions inside a laboratory environment are to be simulated, a free convection coefficient of h = 10 W/m^2K is considered. The main objective of modelling results is to analyze the influence of the background temperature, laser placement and laser power on the crack detection.

Table 11: Material Properties of CeO_2 [49] and Model/Crack Dimensions

Material Property (CeO_2)	**Model Dimensions (Cylinder)**
$k = 6\frac{W}{mK}$, $\rho = 7600\frac{kg}{m^3}$, $c = 390\frac{J}{kg.K}$	Diameter = 1.8 cm, Thickness = 0.8 cm

Table 12: Boundary Conditions/Governing Equation pertaining to thermal modelling of cracked CeO_2 Model shown in Figure 52

Heating Configuration	**Boundary Condition (B.C.)**	**Governing Equation**
Uniform point surface heating with a laser (Steady State)	$q'' = Q_0 \frac{\exp\left(-\frac{r^2}{2R_0^2}\right)}{\sqrt{2\pi R_0^2}}$ top surface $q'' = h(T - T_b)$ other surfaces	$k\nabla^2 T = 0$

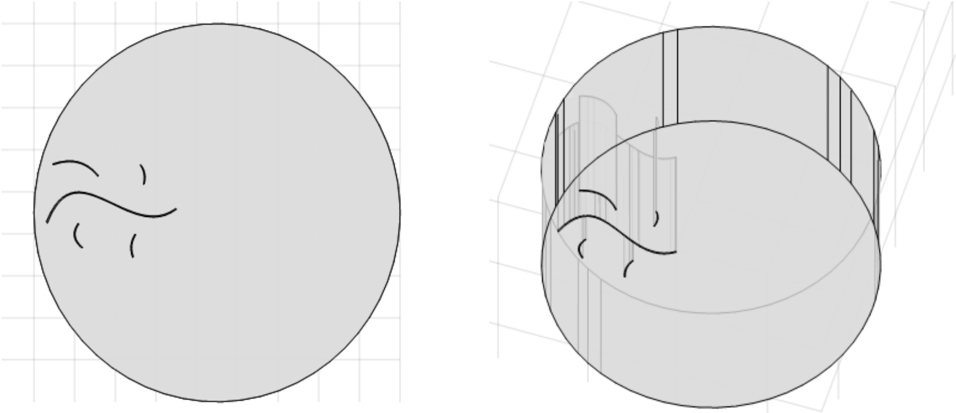

Figure 54: Cracked CeO_2 Model with radial and longitudinal through cracks

5.2 Influence of laser placement

The preliminary set of modelling results highlight the effect of laser placement. Figure 55, 56, 57 showcase modelling IR imaging results using laser heating at locations (X), (Y), (Z) on the sample.

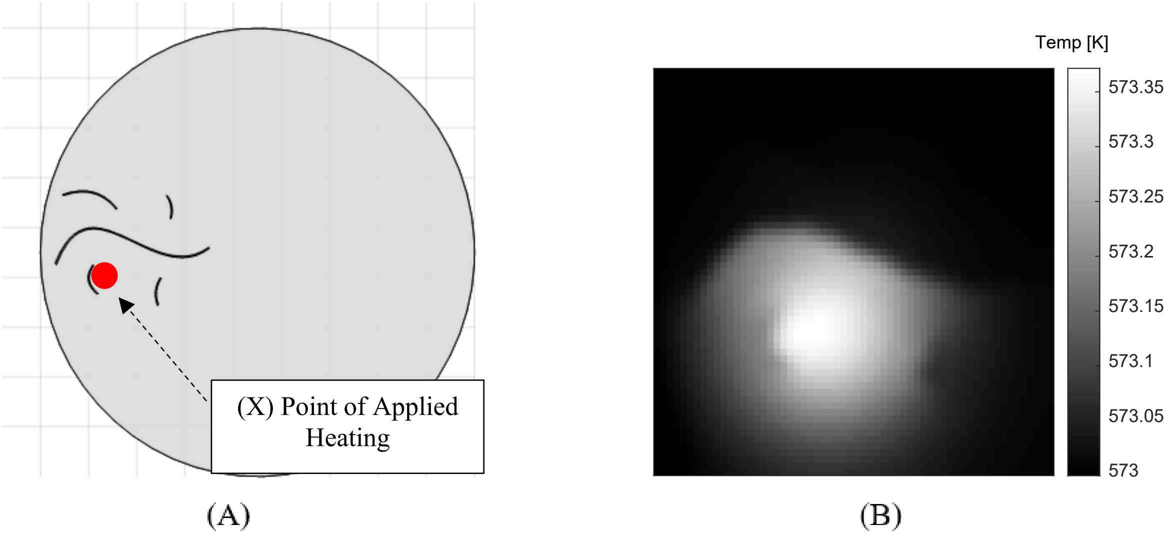

Figure 55: Modelling IR imaging results using laser heating at location (X) on cracked geometry

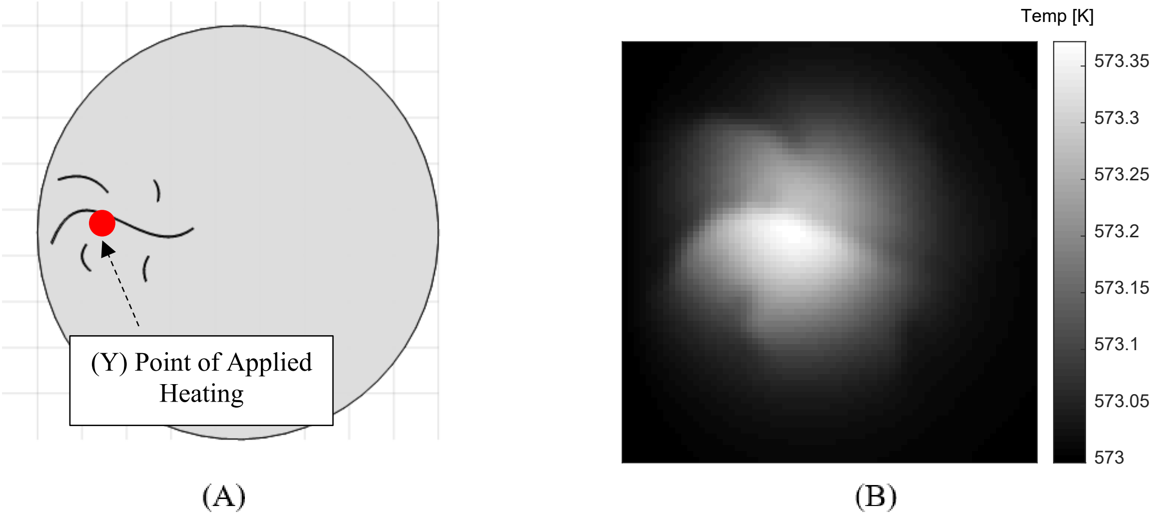

Figure 56: Modelling IR imaging results using laser heating at location (Y) on cracked geometry

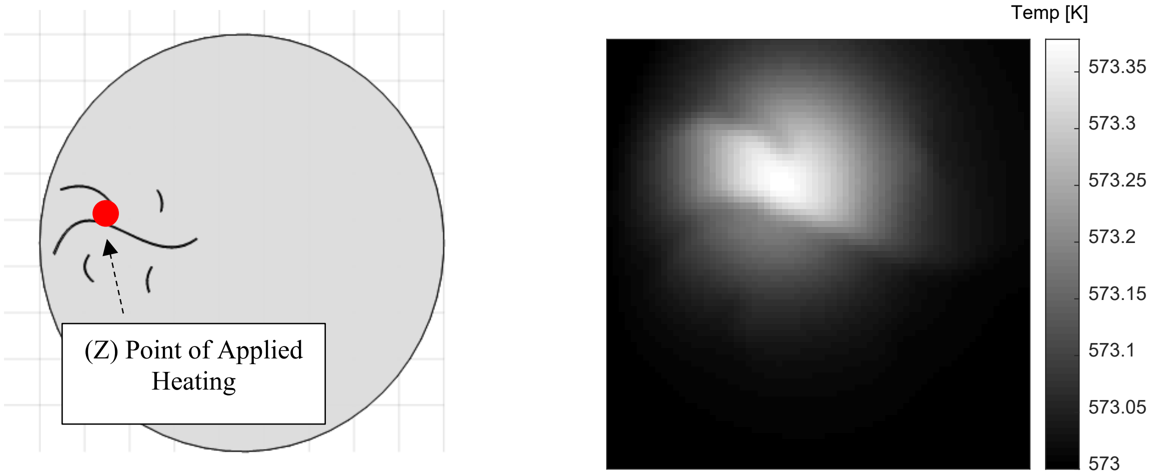

(A) (B)

Figure 57: Modelling IR imaging results using laser heating at location (Z) on cracked geometry

Comparing all the three configurations, only laser heating position (Z) corresponding to Figure 56, outputs all the crack features evenly with reasonable contrast. IR imaging plots results shown in Figures 55 and 56 display only certain crack features located in the vicinity of the point of applied heating. The imaging results indicate that depending on the laser placement, different crack features become more apparent. The cracks located in the vicinity of the point of applied heating display better visibility as compared to cracks which are far away. There are mainly two reasons why a feature may not be apparent using laser heating. Having the laser relatively far from the feature, and having the laser directly on the feature. Having the laser far from the feature does not create enough heat on the feature to emit perceptible blackbody radiation and if it is emitting perceptible blackbody radiation, the heat gradient across the feature is not sufficient to get the contrast. Having the laser directly on the feature heats the feature sufficiently to emit blackbody radiation, but heats the feature evenly across the feature to not create any contrast.

5.3 Influence of background temperature and laser power

The next set of modelling results highlight the effect of background heat and laser power on the IR imaging results. The $\mathrm{CeO_2}$ modelling results are presented from $T_b = 100^o C$ to 300^o C with 50^o C increments. Figure 56 shows the modelling IR images at various background temperatures combined with the laser heating.

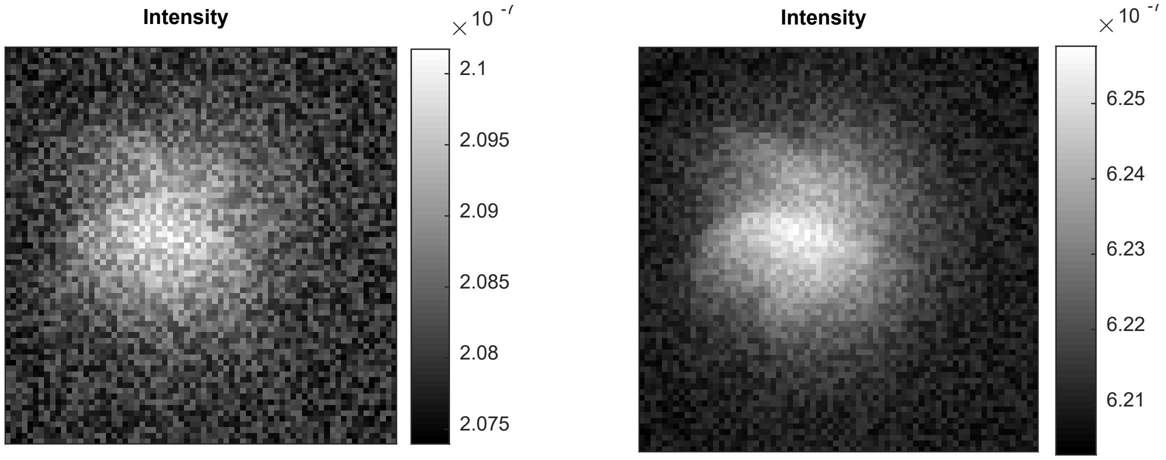

(a) $T_b = 100^\circ C, P_{laser} = 200\,mW$

(b) $T_b = 150^\circ C, P_{laser} = 200\,mW$

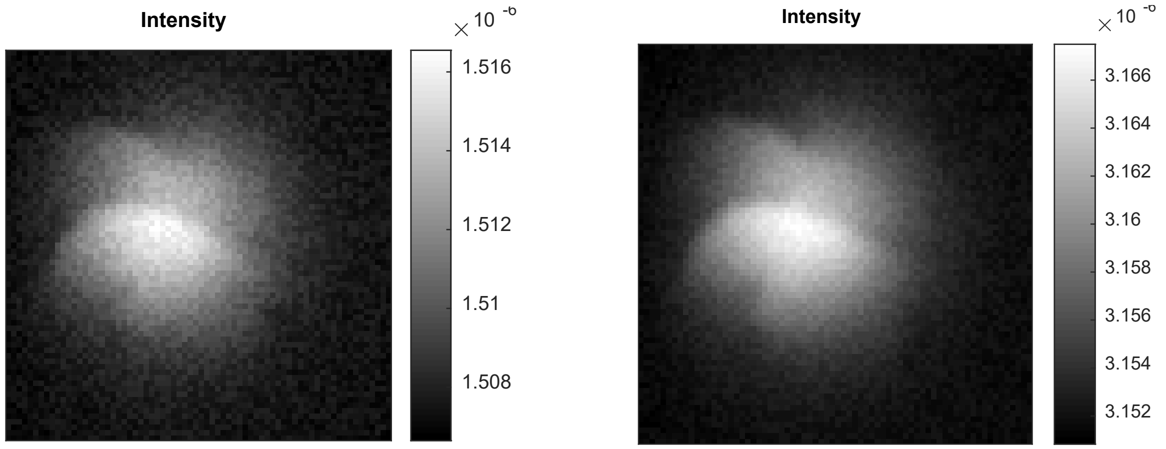

(c) $T_b = 200^\circ C, P_{laser} = 200\,mW$

(d) $T_b = 250^\circ C, P_{laser} = 200\,mW$

Figure 58: IR imaging results (combined heating of furnace,laser), configuration (a) – (d)

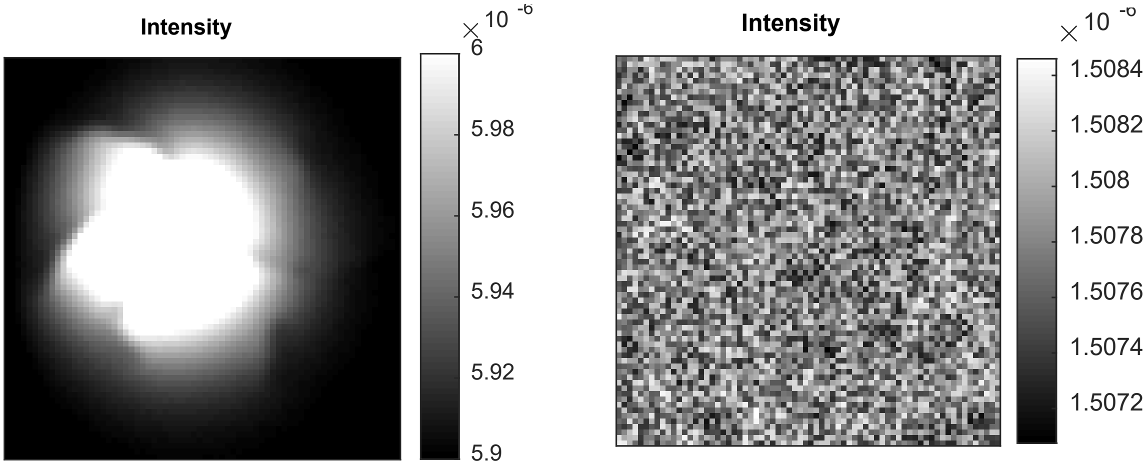

(e) $T_b = 200° \, C, P_{laser} = 2.5 \, W$ (f) $T_b = 300° \, C, P_{laser} = 0 \, W$

Figure 58 (contd): IR imaging results (combined heating of furnace,laser), configuration (e) – (f)

Initially considering Figure 58 (a), the operating conditions are, $T_b = 100° \, C$ and $P_{laser} = 200 \, mW$. Here we observe noise/distortion due to a low background temperature and hence the crack features are distorted due to the camera noise. For Figures 58 (b) with an elevated background temperature of $T_b = 150° \, C$, the crack features are more clearly visible as compared to case (a). However in case (b) there are still traces of noise and distortion. For Figure 58 (c) with a high background temperature of $T_b = 200° \, C$, the crack features are clearly visible with almost no traces of noise and distortion. The case (d) results with a high background temperature of $T_b = 250° \, C$ are similar to the results for case (c). Considering Figure 58(e) with $T_b = 300° \, C, P_{laser} = 2.5$, the crack features are not visible in the IR images. This can be attributed to the high heating power value with induces a high contrast in the IR thermal image. Note that for Figure 58(e), the minimum and maximum value of the radiation intensity is $6 \times 10^{-9} \, W$ and $7.5 \times 10^{-9} W$

respectively. However for Figure 58(d) where crack features are visible with a reasonable contrast, the minimum and maximum radiation intensity values are 1.254×10^{-9} W and 1.27×10^{-9}W respectively. IR images are limited due to the dynamic range and hence are unable to efficiently transfer thermal targets having a high thermal contrast. Finally considering Figure 58 (f) with $\mathrm{T_b} = 300° \mathrm{C}, \mathrm{P_{laser}} = 0 \mathrm{W},$ no crack features are visible and the signal is distorted. This can be attributed to the zero value of the laser heating power. Although a high background temperature is present, there is no contrast induced and the crack model is uniformly heated throughout the surface.

5.4 Summary and Conclusion

IRT technology is a mature and powerful nondestructive evaluation approach for characterizing a wide variety of structural behaviors in materials in many industries. Even so, to date, in-pile applications have benefited little from its utility, likely in part due to engineering and materials challenges related to obtaining optical images in a reactor environment. As a preliminary step, an emphasis has been placed to evaluate possible configurations for crack detection under laboratory environment and in-pile configurations. Lock in thermography, a form of an active IRT technology has been identified as the promising methodology for achieving in-pile applications. A detailed modeling study has been performed for the IR thermal imaging considering the details of infrared thermal modelling (Chapter 2), fiber bundles (Section 3.1), camera detector system (Section 3.2) and the lock in module (Section 3.3).

Modeling results shows that IR thermography can observe cracks in both the in-pile and laboratory conditions (Chapter 4). For the in-pile modelling, results and discussions for two different heating configurations have been presented. The configuration in case A, B are targeted for the in-pile IR imaging under steady state and lock in conditions respectively. Imaging under both configurations is performed using optical IR fiber bundles which acts a medium to carry optical information. A crack thermal model has been developed and the radiation intensity profiles have been generated for background temperatures from 300 K – 1000 K. There are several limiting parameters which distort the crack features in the radiation intensity profiles under the in-pile configuration: - IR Camera (NETD and NEP), optical IR fiber bundles (Attenuation and Dispersion), Optical System (Distortion) and the harsh environment inside the reactor core which induces an additional noise, attenuation and dispersion.

For the surface heating model under the laboratory conditions, results and discussions for two different heating configurations have been presented. The configuration in case C, D are targeted for IR imaging under steady state and lock in conditions respectively. Here the radiation intensity profiles have been generated for background temperatures from 300 K – 1000 K. The limiting parameters which distort the crack features in the radiation intensity profiles under laboratory conditions are: - IR Camera (NETD and NEP) and the Optical System (Distortion).

The Signal to Noise Ratio has been used as a parameter to quantify the crack visibility in the IR radiation intensity profiles. For SNR < 1, the signal is distorted/noisy and the crack features are not visible. For SNR > 1, the crack is quantifiable as the signal gets amplified and has a greater magnitude than the noise/distortion. Figure 52 (Section 4.3) summarizes the results for the in-pile (Case (A), (B)) and steady state configurations (Case (C), Case (D)). Higher SNR values are obtained for the laboratory configurations (Case (C), (D)) as compared to the in-pile configurations (Case (A), (B)). This can be attributed to the additional noise and dispersion losses in the in-pile cases due to the optical fiber bundles and the harsh reactor environment. Further comparing the steady state and lock in cases, higher SNR values are obtained for the lock in configuration. This can be attributed to the lock in mechanism which fits the input signal to a reference signal and outputs a relatively smooth signal with little traces of noise and distortion. Overall the modelling results show the feasibility of using IR thermography in fuel rod monitoring in nuclear cores and in laboratory environments. An additional IR modelling study has been performed on realistic crack models. A thermal model has been developed for the same with the appropriate governing equations and boundary conditions. The preliminary set of modelling results focus on the effect of laser placement for crack imaging, while the latter set of results highlight the effect of furnace heat (background heat) on the IR imaging.

Progress towards the goal of real time imaging is very promising and work still needs to be done on optimizing the modelling methodology. Moreover focus should also be placed on development of integrated measurement systems which provide characterization of material properties, chemistry and microstructure evolution [50]. The following areas are for the development of integrated measurement systems for nuclear fuel and materials: -

- Thermal properties: thermal conductivity (photothermal radiometry, three-omega sensor, and needle probe) [4], [51]
- Mechanical properties: creep testing systems (LVDT, strain gauges); radial swelling (diameter gauge, electrochemical impedance); crack growth and void formation (direct current potential drop; thermography) [2], [52], [53], [54], [55]
- Chemistry: hydride formation and corrosion (electrochemical impedance spectroscopy, electrochemical corrosion potential); crud build-up (diameter gauge) [56]
- Microstructure: recrystallization (resonant ultrasound spectroscopy) [57]

The ultimate aim is to integrate a complete experimental system to create a full in-reactor experiment and develop infrared thermography (IRT) approach for in-reactor monitoring of the fuel behavior.

Bibliography

1. MEINLSCHMIDT, P. and J. ADERHOLD, *Thermographic Inspection of Rotor Blades* Proceedings on the 9th European Conferences on NDT, September 2006.
2. Hurley, D., et al., *FY-17 Status Report for the Development of Infrared Thermography for In-Pile Fuel Behavior Applications.* Idaho National Laboratory, September 2017.
3. Agarwal, K., et al., *Infared Thermography for in-pile imaging of Nuclear Fuel Cracking.* 11th Nuclear Plant Instrumentation, Controls and Human-Factor and Machine Interfaces, Orlando, FL, 2019.
4. Fleming, A., et al., *FY-17 Report for the design of a benchtop Phothothermal Radiometry system.* Idaho National Laboratory, Idaho Falls (INL/EXT-17-43412) 2017.
5. AMAYA , M., J. NAKAMURA, and T. FUKETA, *Measurements of Crystal Lattice Strain and Crystallite Size in Irradiated UO2 Pellet by X-ray Diffractometry.* Journal of Nuclear Science and Technology, 2008. **45:3, 244-250**.
6. Oguma, M., *Cracking and relocation behavior of nuclear fuel pellets during rise to power.* Nuclear Engineering and Design, 1983. **76**(1): p. 35-45.
7. Riyad, F., *Simultaneous analysis of Lattice Expansion and Thermal Conductivity in Defected Oxide Ceramics.* Electronic Thesis or Dissertation. Ohio State University, 2017.
8. Pankaskie, P.J., *The Impact of Pellet-Cladding Interaction on Fuel Integrity.* February 1978.

9. Mishra, P., et al., *Microstructural observations of degradation of fuel and cladding in defective fuel pins during reactor operation.* BARC

10. Khvostov, G., *Modeling of central void formation in LWR fuel pellets due to high-temperature restructuring.* Nuclear Engineering and Technology, October 2018. **50**(7): p. 1190-1197.

11. Spencer, B., et al., *Discrete Modeling of Early-Life Thermal Fracture in Ceramic Nuclear Fuel* Idaho National Laboratory, 2014. **WRFPM**.

12. Khafizov, M., et al., *Investigation of thermal transport in composites and ion beam irradiated materials for nuclear energy applications.* J. Mater, 2016. **Res. 32, 204**.

13. Ashraf, M.M. and A.R. Khan, *Review Of Neutron Radiographic Applications In Industrial and Biological Systems.* Non Destructive Testing Group, October 1992.

14. Berger, H. and F. Iddings, *Neutron Radiography.* Non Destructive Testing Information Analysis Center, 1985.

15. Beer de, F.C., *Neutron- and X-ray radiography/tomography: non-destructive analytical tools for the characterization of nuclear materials.* The Journal of The Southern African Institute of Mining and Metallurgy, October 2015. **115**.

16. Korsah, K., et al., *Assessment of Sensor Technologies for Advanced Reactors.* ORNL/TM-2016/337 R1.

17. Primer, C., et al., *Digital Environment for Advanced Reactors Workshop.* INL/EXT-18-46051, 2018.

18. Calderoni, P. and C. Jensen, *In-pile Instrumentation Strategic Plan.* INL/EXT-18-51432, 2018.

19. Hurley, D., B. Halbert, and P. Calderoni, *In-Pile Instrumentation Initiative: A Multidisciplinary Scientific Approach for Characterization of Fuels and Materials.* INL/EXT-17-43366.

20. Castanedo, C.I., et al., *Comparative Study of Active Thermography Techniques for the Non-Destructive Evaluation of Honeycomb Structures.* Research in Nondestructive Evaluation, 2009: p. 1-31.

21. TOMIĆ, L.D., et al., *Application of Plused Flash Thermography Method for Specific Defect Estimation in Amuminum.*

22. Candoré, J.C., et al., *Nondestructive testing of works of art by stimulated infrared thermography.* European Physical Journal: Applied Physics, EDP Sciences, 2012.

23. Szwedo, M. and P. Hellstein, *Qualitative diagnostics of wind-turbine blades inspection using active thermography.* Quantitative Infrared Thermography, 2014.

24. Streza, M., et al., *Infrared lock - in thermography for surface defect imaging in metals for industrial diagnosis.* Quantitative InfraRed Thermography, 2014.

25. Ranjit, S., K. Kang, and W. Kim, *Investigation of lock-in infrared thermography for evaluation of subsurface defects size and depth.* International Journal of Precision Engineering and Manufacturing, October 2015. **16**(11): p. 2255-2264.

26. Yang, J. and S. Hwang, *Multi-spot laser lock-in thermography for real-time imaging of cracks in semiconductor chips during a manufacturing process.* Journal of Materials Processing Technology, March 2016. **229**: p. 94 - 101.

27. Breitenstein, O. and H. Straube, *Lock-in Thermography Investigation of Solar Modules.* 26th European Photovoltaic Solar Energy Conference and Exhibition.

28. Breitenstein, O., C. Schmidt, and F. Altmann, *Application of Lock-In Thermography to failure and analysis in integrated circuits.* Microtherm, 2011.

29. Guo, X. and V. Vavilov, *Crack detection in aluminum parts by using ultrasound-excited infrared thermography.* Infrared Physics & Technology, November 2013. **61**: p. 149 - 156.

30. Li, N., et al., *A real-time infrared imaging simulation method with physical effects modeling of infrared sensors.* Infrared Physics & Technology, September 2016. **78**: p. 45-57.

31. Dirnwober, M., *Characterization of Optical Fibers in the Mid-Infrared.* May 2005.

32. Klimenko, A.V. and V.M. Zorin, *Thermal and Nuclear Power Plants/Handbook.* MEI Press, 2003.

33. Incropera, F. and D.P. DeWitt, *Fundamentals of heat and mass transfer.* New York: J Wiley, 2002.

34. Vollmer, M. and K.P. Mollmann, *Infrared Thermal Imaging.* European Journal of Physics, 2007.

35. Usamentiaga, R., et al., *Infrared Thermography for Temperature Measurement and Non-Destructive Testing.* Sensors, 2014.

36. Petrie, C.M., *Fiber Optic Instrumentation in High Temperature Irradiation Environments.* Oak Ridge National Laboratory.

37. *Fiber Optics Handbook.* Optical Society of America, McGraw - Hill.

38. Senior, J.M., *Optical Fiber Communications Principles and Practice.* Prentice Hall.

39. Gal, U., et al., *Coherent hollow-core waveguide bundles for thermal imaging.* Applied Optics, September 2010. **49**(25).

40. Tzannes, A.P. and J.M. Mooney, *Measurement of the modulation transfer function of infrared cameras.* SPIE Optical Engineering, June 1995. **34**.

41. Girard, S., P. Paillet, and N. Richard, *Combined High Dose and Temperature Radiation Effects on Multimode Silica-Based Optical Fibers.* IEEE TRANSACTIONS ON NUCLEAR SCIENCE, December 2013. **60**.

42. Petrie, C.M., *Characterization of the Performance of Sapphire Optical Fiber in Intense Radiation Fields, when Subjected to Very High Temperatures.* The Ohio State University, Columbus, OH, 2014.

43. Sánchez, I.G., D.V. Ras, and T.A. Birks, *The Airy fiber: an optical fiber that guides light diffracted by a circular aperture.* Optica, 2016. **3**(3): p. 270 - 276.

44. Holst, G., *Common Sense Approach to Thermal Imaging.* SPIE OPTICAL ENGINEERING, 2000.

45. Bhattacharyya, S., et al., *Implementation of Digital Lock-in Amplifier.* Journal of Physics, 2016.

46. Kozlowski, L.J. and W.F. Kosonocky, *Infrared Detector Arrays.* Imaging Detectors.

47. Löf, J. and J. Dehlin, *Dynamic Infrared Simulation: A Feasibility Study of a Physically Based Infrared Simulation Model.* 2006.

48. Kennedy, H., *Modelling noise in thermal imaging systems.* Proc SPIE 1969, Infrared Imaging Systems : Design, Analysis, Modeling and Testing, August 1993.

49. Khafizov, M., et al., *Measurement of thermal conductivity in nanocrystalline ceria.* Journal of the American Ceramic Society, 2014.

50. Calderoni, P. and C. Jensen, *In-Pile Instrumentation Strategic Plan.* Idaho National Laboratory, 2018. **INL/EXT-18-51432, Revision 1**.

51. Hurley, D., et al., *Local measurement of thermal conductivity and diffusivity.* Review of Scientific Instruments 2015.

52. Schley, R., D. Hurley, and Z. Hua, *Optical fiber technique for in-reactor mechanical properties measurement.* AIP Conference Proceedings 1511, 2013.

53. Jensen, C., et al., *FY17 Report for Instrumentation Development for the Transient Testing Program* Idaho National Laboratory, September 2017.

54. Rempe, J., et al., *Enhanced in-pile instrumentation at the Advanced Test Reactor.* 2nd International Conference on Advancements in Nuclear Instrumentation, Measurement Methods and their Applications, 2011.

55. Daw, J., et al., *Ultrasonic Thermometry for In-Pile Temperature Detection* Nuclear Plant Instrumentation, Control and Human-Machine Interface Technologies 2010.

56. Kadiri, H., et al., *Transformations and cracks in zirconia films leading to breakaway oxidation of Zircaloy.* Acta Materialia, June 2013. **61**(11): p. 3923-3935.

57. Hurley, D., S. Resse, and F. Farzbod, *Application of laser-based resonant ultrasound spectroscopy to study texture in copper.* Journal of Applied Physics, 2012. **111**(5).